

©Copyright 2019

M. P. Ross

# Precision Mechanical Rotation Sensors for Terrestrial Gravitational Wave Observatories

M. P. Ross

A dissertation  
submitted in partial fulfillment of the  
requirements for the degree of

Doctor of Philosophy

University of Washington

2019

Reading Committee:

Name of Chairperson, Chair

First committee member

Next committee member

etc

Program Authorized to Offer Degree:  
Physics

University of Washington

**Abstract**

Precision Mechanical Rotation Sensors for Terrestrial Gravitational Wave Observatories

M. P. Ross

Chair of the Supervisory Committee:  
Title of Chair Name of Chairperson  
Department of Chair

# TABLE OF CONTENTS

	Page
List of Figures . . . . .	iii
Chapter 1: Introduction . . . . .	2
1.1 Gravitational Wave Theory . . . . .	2
1.1.1 Linearized General Relativity . . . . .	2
1.1.2 Compact Binary Coalescence . . . . .	3
1.2 LIGO . . . . .	5
1.2.1 Sensitivity . . . . .	5
1.2.2 Events . . . . .	7
1.3 Seismic Isolation . . . . .	8
1.3.1 LIGO Scheme . . . . .	8
1.3.2 Internal Seismic Isolation . . . . .	9
1.3.3 Sensor Correction . . . . .	10
Chapter 2: 1-m Scale Ground Rotation Sensors . . . . .	12
2.1 Tilt Contamination . . . . .	12
2.2 Sensor Correction with Tilt Subtraction . . . . .	13
2.3 Mechanical System . . . . .	15
2.4 Multi-Slit Autocollimator Readout . . . . .	18
2.5 Controls . . . . .	20
2.6 Noise Performance . . . . .	21
2.7 Hanford Installation . . . . .	23
2.8 Livingston Installation . . . . .	23
2.9 Duty Cycle Improvements . . . . .	25
Chapter 3: 30-cm Scale On-Board Rotation Sensors . . . . .	29
3.1 Angular Controls . . . . .	29

3.2	Isolation Scheme . . . . .	32
3.3	Projected Angular Control Improvements . . . . .	32
3.4	Mechanical System . . . . .	32
3.5	Interferometric Readout . . . . .	32
3.6	Mass Adjustment . . . . .	41
3.7	Controls . . . . .	42
3.8	Noise Performance . . . . .	42
Chapter 4:	Applications . . . . .	44
4.1	Geophysics . . . . .	44
4.1.1	Rayleigh Wave Theory . . . . .	44
4.1.2	Wave Field Parameter Extraction . . . . .	45
4.1.3	single Station Dispersion Measurements . . . . .	46
4.2	Newtonian Noise . . . . .	48
4.2.1	Theory . . . . .	48
4.2.2	Observations . . . . .	48

## LIST OF FIGURES

Figure Number		Page
2.1	Ground motion spectra recorded at the X end station of the Hanford Observatory during low and high winds. Below 100 mHz, wind driven tilts become dominate during high winds. From 100 mHz to 1 Hz the spectra are dominated by the oceanic microseism while above 1 Hz the seismic motion is sourced by local athropogenic activity. . . . .	14
2.2	CAD rendering of the Beam Rotation Sensor with the vacuum and optical readout systems omitted. The bem with its two brass end masses can be seen through the thermal shielding, shown here as transparent. . . . .	16
2.3	Noise budge for the Beam Rotation Sensors where the blue curve shows the performance at a quiet time, in red is the motion of the reference mirror which can be regarded as an estimate of the readout noise, yellow shows an estimate of the thermal noise, purple shows the noise from the capacitive actuators, and green shows the some of all known noise sources. . . . .	22
2.4	Representative amplitude spectral density showing the tilt subtraction during windy conditions achieved at End-X of LHO where blue is the BRS signal multiplied by $g/\omega$ , read is the raw seismometer signal, and yellow is the tilt corrected signal. Similar perform has been achieved by all of the installed BRSs. . . . .	24
2.5	Time series showing the tilt subtraction at End-X of LHO where blue is the BRS signal multiplied by $g/\omega$ , read is the raw seismometer signal, and yellow is the tilt corrected signal. As can be seen, the tilt subtraction removes a collection of transients, likely due to the gusts of wind. . . . .	25
2.6	. . . . .	26
2.7	. . . . .	28
3.1	Performance of the current angular sensing and control system. . . . .	30
3.2	Theoretical noise curves for the cBRS, blue, and seismometer pair located 1-m apart. . . . .	31
3.3	Projected rotational performance of Stage 2 of the ISI with, yellow, and without, red, the cBRS. Also shown is the input ground tilt model, blue, which represents the observed tilt during windy times. . . . .	33

3.4	Projected translational performance of Stage 2 of the ISI with, yellow, and without, red, the cBRS. Also shown is the input ground motion model, blue, which represents the observed tilt during windy times. The control loops here can be tuned to decrease motion at $\sim 100$ mHz, the microseism frequencies, by increasing motion at $\sim 10$ mHz and vice versa. . . . .	34
3.5	Projected performance of the angular sensing and control system with the seismic performance described in Section 3.2. . . . .	35
3.6	Projected performance of the angular sensing and control system with the seismic performance described in Section 3.2. . . . .	36
3.7	Projected low frequency strain noise with and without the cBRS. The blue line is the current sensitivity of LLO, the orange is the aLIGO design sensitivity, green is the modeled noise contribution of the current ASC system, and red is the improved ASC noise contribution with the seismic isolation described in Section 3.2. . . . .	37
3.8	CAD rendering of the compact BRS (cBRS) showing the cross with its copper end masses which is hung from the flexures from the surrounding support structure. Additionally, the translation stages which hold the fiber interferometer readouts can be seen on either end of the support below the two horizontal end masses. . . . .	39
3.9	. . . . .	40
3.10	. . . . .	41
3.11	. . . . .	43
4.1	Rayleigh wave phase velocity measurements made by instruments located at the End-Y station of LHO, blue, and the same measurements achieved by the array of seismometers deployed at LHO. Each line represent the measurements achieved by different earthquakes. The angle of incidence of each wave was measured independent of the single station and used within the analysis. <b>cite tilt seismology</b> . . . . .	47

# DEDICATION

To Grace



The first observation showed ... that owing to the extreme sensitiveness of the instrument to vibrations, the work could not be carried on during the day. The experiment was next tried at night. ... so extraordinarily sensitive was the instrument that the stamping of the pavement, about 100 meters from the observatory, made the fringes disappear entirely!

If this was the case with the instrument constructed with a view to avoid sensitiveness, what may we not expect from one made as sensitive as possible!

---

*Albert A. Michelson*

*“The Relative Motion of the Earth and  
the Luminiferous Ether”*

## Chapter 1

# INTRODUCTION

### 1.1 Gravitational Wave Theory

#### 1.1.1 Linearized General Relativity

In early twentieth century, Einstein formulated the theory of General Relativity, which supplanted the static space-time in which all prior physics was formulated in, with a deformable space-time which gave a geometric explanation for gravity. This space-time is described by a unitless tensor field,  $g_{\mu\nu}$ , called the metric [5]. The deformation of this metric follows the Einstein equation:

$$R_{\mu\nu} - \frac{1}{2}R g_{\mu\nu} + \Lambda g_{\mu\nu} = \frac{8\pi G}{c^4}T_{\mu\nu} \quad (1.1)$$

where  $R_{\mu\nu}$  is the Riemann tensor,  $R$  is the Ricci scalar,  $\Lambda$  is the cosmological constant,  $G$  is the gravitational constant,  $c$  is the speed of light, and  $T_{\mu\nu}$  is the stress energy tensor.

If one focuses on a locally flat region of space which is much smaller than the scale of the universe, then the cosmological constant term can be sent to zero and the metric can be approximated via [? ]:

$$g_{\mu\nu}(\vec{x}, t) \approx \eta_{\mu\nu}(\vec{x}, t) + h_{\mu\nu}(\vec{x}, t) \quad (1.2)$$

where  $\eta_{\mu\nu}$  is the flat Minkowski metric and  $h_{\mu\nu}$  is a small perturbation<sup>1</sup>,  $|h_{\mu\nu}| \ll 1$ . Applying the Einstein equation and transferring to a transverse-traceless coordinate system yields the wave equation:

$$\square h_{\mu\nu} = -\frac{16\pi G}{c^4}T_{\mu\nu} \quad (1.3)$$

---

<sup>1</sup>The largest amplitude of gravitational wave strain measured thus far is on the order of  $|h_{\mu\nu}| \approx 10^{-21}$ [? ]

For a complete derivation see Reference [? ]. Vacuum solutions propagating along the  $z$ -axis can readily be found as:

$$h_{ij}(t, x) = \begin{pmatrix} h_+ & h_\times & 0 \\ h_\times & -h_+ & 0 \\ 0 & 0 & 0 \end{pmatrix} \cos(\omega t - \kappa z) \quad (1.4)$$

where  $h_+$  and  $h_\times$  are the amplitudes in the “plus” and “cross” polarizations<sup>2</sup>,  $\omega$  is the angular frequency of oscillation, and  $\kappa$  is the wavenumber. Here  $i$  and  $j$  run from 1 to 3 and correspond to the the three spacial coordinates. The time components are suppressed as the  $h_{0\nu}$  components are zero due the coordinate choice and  $h_{00}$  is zero outside the source.

### 1.1.2 Compact Binary Coalescence

As of writing, the only systems to have been observed to emit gravitational waves are composed of two compact<sup>3</sup> objects orbiting a common center of mass, so called compact binaries. These objects could be neutron stars, as with the Hulse-Taylor binary pulsar[? ] and GW170817[? ], or black holes like GW150914[? ] and most events in the GWTC-1[2].

Such a system can be treated as two point masses,  $m_{1,2}$  in a Keplerian orbit which decays due to the emission of gravitational waves. The gravitational waves emitted by such a system

---

<sup>2</sup>A massless graviton is assumed here. A massive graviton would yield five polarizations instead of two. Current graviton mass constraints are  $m_g < 7.7 \times 10^{-23} \text{eV}/c^2$  [? ]

<sup>3</sup>The compactness of the objects are importance only to satisfy a point mass approximation and to allow observation in current instruments. Non-compact objects such as white and brown dwarfs will emit gravitational waves in their inspiral phase but merge due to Roche lobe overflow long before entering the frequency band accessible today.

can be shown to be:

$$h_+(t) = \frac{4}{r} \left( \frac{GM}{c^2} \right)^{5/3} \left( \frac{\pi f}{c} \right)^{2/3} \frac{1 + \cos^2 \theta}{2} \cos(\omega t + \phi) \quad (1.5)$$

$$h_\times(t) = \frac{4}{r} \left( \frac{GM}{c^2} \right)^{5/3} \left( \frac{\pi f}{c} \right)^{2/3} \cos \theta \quad (1.6)$$

$$\sin(\omega t + \phi) \quad (1.7)$$

where  $M = (m_1 m_2)^{3/5} / (m_1 + m_2)^{1/5}$  is the chirp mass,  $r$  is the distance to the center of mass of the source,  $\theta$  is the viewing angle,  $f = \omega/2\pi$  is the frequency of oscillation, and  $\phi$  is the initial phase of the system.

The emission of these gravitational waves carry energy away from the system and thus the orbit decays. As the radius of the orbit decreases the frequency of oscillation must grow due to Kepler's law. This then causes the amplitude of the emitted gravitational waves to grow and the orbit to decay quicker. The frequency change during this run away process can be shown to be:

$$\dot{f} = \frac{96}{5} \pi^{8/3} \left( \frac{GM}{c^3} \right)^{5/3} f^{11/3} \quad (1.8)$$

This process produces a characteristic “chirp” signal which begins as low frequency and amplitude then grows in amplitude while shifting to higher frequency. The signal culminates in a final sharp increase in both frequency and amplitude before the objects merger. This can be seen in Figure ?? which shows a spectrogram of the observed strain at the LIGO observatories for GW170817.

### **include figure of GW170817**

Although binary systems are the topic of choice here, many other systems should theoretically emit gravitational waves. These can range from asymmetric spinning stars and supernova to cosmic strings and density perturbations in the early universe. With the measurement of gravitational waves, humankind technologically expand our senses to include the faint vibrations of space-time. This ability has expanded the types of astronomical systems we can study and may one day allow further insight into the beginning of the universe.

## 1.2 *LIGO*

### 1.2.1 *Sensitivity*

The Laser Interferometric Gravitational wave Observatory (LIGO) is a pair of 4 km long L-shaped interferometric gravitational wave detectors, one located in Hanford, Washington (LHO) and the other in Livingston, Louisiana. Each observatory is a dual-recycled Fabry-Perot Michelson interferometer which measures the differential strain between its two arms formed by pairs of partially reflective mirrors, also called test masses.

**include LIGO schematic**

As a gravitational wave passes the observatory, the arms experience a strains that follow

[? ]:

$$h_{xx} = h_+ ( \quad (1.9)$$

$$\cos^2 \theta \quad (1.10)$$

$$\cos^2 \phi - \quad (1.11)$$

$$\sin^2 \phi) + 2 h_{\times} \quad (1.12)$$

$$\cos \theta \quad (1.13)$$

$$\sin \phi \quad (1.14)$$

$$\cos \phi \quad (1.15)$$

$$h_{yy} = h_+ ( \quad (1.16)$$

$$\cos^2 \theta \quad (1.17)$$

$$\sin^2 \phi - \quad (1.18)$$

$$\cos^2 \phi) - 2 h_{\times} \quad (1.19)$$

$$\cos \theta \quad (1.20)$$

$$\sin \phi \quad (1.21)$$

$$\cos \phi \quad (1.22)$$

$$h = \frac{1}{2}(h_{xx} - h_{yy}) = \frac{1}{2}h_+ (1 + \quad (1.23)$$

$$\cos^2 \theta) + h_{\times} \quad (1.24)$$

$$\cos \theta \quad (1.25)$$

$$\sin 2\phi \quad (1.26)$$

where  $h_{xx}$  and  $h_{yy}$  are the strain along the x and y arm respectively,  $\theta$  and  $\phi$  are the polar and azimuthal angles of the direction of propagation, and  $h$  is the differential strain as measured by the observatory.

The complex series of optics allows the observatory to measure differential strains down to  $10^{-23}$  **at 40 Hz**. A noise curve for **some** observatory is shown in Figure ?? where one can see that the sensitive band of the observatory runs from **30 Hz up to 16 kHz**. At low frequencies the noise is dominated by residual control noise while at high it is dominated by noise caused by quantum fluctuations.

**include LIGO strain curve**

### 1.2.2 *Events*

With the current sensitivity the primary systems of interest are compact binaries, discussed in Section 1.1.2, which merger within the band of interest. A equal mass  $200 M_{\odot}$  binary black hole system would merger at **11 Hz** while a  $1.4 M_{\odot}$  binary neutron star system mergers at **1.5 kHz** yet emits appreciably while sweeping through the LIGO band.

During the first and second observing runs of LIGO, ten binary black hole systems and one binary neutron star merger were detected with high significance. [2] The black holes ranged from  $7 M_{\odot}$  **to**  $120 M_{\odot}$  and merged at distances from **100 Mpc to 2 Gpc**. The neutron star binary was composed of a  $1.2 M_{\odot}$  **and a**  $1.4 M_{\odot}$  at **1 Mpc**. These systems are tabulated in Table ??.

Event Name	m1 ( $M_\odot$ )	m2 ( $M_\odot$ )	$M_f$ ( $M_\odot$ )	Distance (Mpc)	z
GW150914	$35.6^{+4.7}_{-3.1}$	$30.6^{+3.0}_{-4.4}$	$63.1^{+3.4}_{-3.0}$	$440^{+150}_{-170}$	$0.09^{+0.03}_{-0.03}$
GW151012	$23.2^{+14.9}_{-5.5}$	$13.6^{+4.1}_{-4.8}$	$35.6^{+10.8}_{-3.8}$	$1080^{+550}_{-490}$	$0.21^{+0.09}_{-0.09}$
GW151226	$13.7^{+8.8}_{-3.2}$	$7.7^{+2.2}_{-2.5}$	$20.5^{+6.4}_{-1.5}$	$450^{+180}_{-190}$	$0.09^{+0.04}_{-0.04}$
GW170104	$30.8^{+7.3}_{-5.6}$	$20.0^{+4.9}_{-4.6}$	$48.9^{+5.1}_{-4.0}$	$990^{+440}_{-430}$	$0.20^{+0.08}_{-0.08}$
GW170608	$11.0^{+5.5}_{-1.7}$	$7.6^{+1.4}_{-2.2}$	$17.8^{+3.4}_{-0.7}$	$320^{+120}_{-110}$	$0.07^{+0.02}_{-0.02}$
GW170729	$50.2^{+16.2}_{-10.2}$	$34.0^{+9.1}_{-11.1}$	$79.5^{+14.7}_{-10.2}$	$2840^{+1400}_{-1360}$	$0.49^{+0.19}_{-0.21}$
GW170809	$35.0^{+8.3}_{-5.9}$	$23.8^{+5.1}_{-5.2}$	$56.3^{+5.2}_{-3.8}$	$1030^{+320}_{-390}$	$0.20^{+0.05}_{-0.07}$
GW170814	$30.6^{+5.6}_{-3.0}$	$25.2^{+2.8}_{-4.0}$	$53.2^{+3.2}_{-2.4}$	$600^{+150}_{-220}$	$0.12^{+0.03}_{-0.04}$
GW170817	$1.46^{+0.12}_{-0.10}$	$1.27^{+0.09}_{-0.09}$	$\leq 2.8$	$40^{+7}_{-15}$	$0.01^{+0.00}_{-0.00}$
GW170818	$35.4^{+7.5}_{-4.7}$	$26.7^{+4.3}_{-5.2}$	$59.4^{+4.9}_{-4.8}$	$1060^{+420}_{-380}$	$0.21^{+0.07}_{-0.07}$
GW170823	$39.5^{+11.2}_{-6.7}$	$29.0^{+6.7}_{-7.8}$	$65.4^{+10.1}_{-7.4}$	$1940^{+970}_{-900}$	$0.35^{+0.15}_{-0.15}$

The ongoing third observing run has had  $\#$  significant candidates:  $\#$  binary black holes,  $\#$  binary neutron stars, and  $\#$  black hole neutron star systems. Although these candidates have not been verified to be true gravitational wave events, they show a significant increase in rate of detection due to both the decreased noise and increased duty cycle achieved for the third observing run.

### 1.3 Seismic Isolation

#### 1.3.1 LIGO Scheme

To operate interferometric observatories that are sensitive to the strains of space time, one must isolate the instrument from all other sources of differential displacement. As the observatories are located on the surface of the earth, one of the dominate sources of such noise is due to ambient seismic motion.

The ambient seismic wave field is continuously excited across a wide frequency range. Between 50 mHz to 1 Hz the ambient spectrum is dominated by the “microseism” which is an always-present feature that is sources by the earth’s oceans. Above 1 Hz, the dominate source



of seismic motion at the observatories is due to local instrumentation. Yet even in locations without any anthropogenic sources, the ground moves at some level at these frequencies. Without isolation, this motion would dominate any measurements with the interferometer and, more practically, would disrupt any attempt at operating the interferometer at its ideal alignment, so called having the interferometer “locked”.

The LIGO observatories solve this issue by employing a multi-stage seismic isolation system formed of both passive and active stages. First from the ground is the Hydraulic External Pre-Isolation (HEPI) system which is formed by four hydraulic actuators which give a small amount of passive isolation and low frequency active isolation. Suspended from this is the Internal Seismic Isolation (ISI) system. This is a dual stage six degree active isolation and is the primary broad band isolation. From the second stage of the ISI is hung the quadruple pendulum, at the bottom of which is a test mass. This provide high frequency passive isolation which decreases the motion of the test mass like  $1/f^8$ , where  $f$  is the frequency of the motion.

### *1.3.2 Internal Seismic Isolation*

The ISI is comprised of two similar stages each suspended from steel blade springs and wires, the first from HEPI and the second from the first. Each stage is controlled using a set of six magnetic actuators whose signal is comprised of a collection of sensors placed on the stage. The motion of the table is sensed with a series of three axis seismometers which allow for sensing of motion with respect to an inertial frame. Two separate models of seismometers are combined to utilized the instruments with the lowest noise is a given frequency band. Above **3 Hz**, Guralp GS13s are used while between **100 mHz to 3 Hz** Trillium T240s are implemented. These two sensors are “blended” together by sending the T240 through a low pass filter and the GS13 through a high pass. The filtered signals are then added together to form the control signal which is sent to the actuators.

This is done in all six degrees of freedom by having three independent seismometers of each type located 1 meter apart. The three translational signals are comprised of the average

of the corresponding seismometer signals, while the three rotational degrees are sensed by the difference of the seismometer divided by the separation.

### **include seismometer noise figure**

Due to the increase in T240 noise below **100 mHz**, a set of Capacitive Position Sensors (CPS) are deployed which sense the relative motion between either the ground and the first ISI stage or the two stages of the ISI. This is then used as the control signal at low frequencies yielding a control that follows:

$$x_{\text{cont}} = F_{LP} (x_p - x_g)_{\text{CPS}} + F_{BP} x_{p, \text{T240}} + F_{HP} x_{p, \text{GS13}} \quad (1.27)$$

where  $x_{\text{cont}}$  is the control signal,  $x_{p,i}$  is the platform motion sensed by the respective sensor,  $x_g$  is the ground motion, and  $F_{LP}$ ,  $F_{BP}$ ,  $F_{HP}$  are respectively a low-pass, band-pass, and high-pass filter. When this filter is utilized in feedback, the residual motion of the platform can be approximated by:

$$x_p(f) \approx F_{LP} (x_g(f) + n_{\text{CPS}}(f)) + F_{BP} n_{\text{T240}}(f) + F_{HP} n_{\text{GS13}}(f) \quad (1.28)$$

where  $n_i(f)$  is the sensor noise spectrum for the relevant sensor. This approximation ignores tilt to horizontal coupling which is address in Sections ??.

### *1.3.3 Sensor Correction*

The isolation can be improved further with the addition of a three axis seismometer, in this case a Struckheisen STS-2, placed on the floor of the observatory. This senses the ground motion and can be used to do so called “sensor correction”. This is procedure of subtracting the ground contribution of the CPS signal to recover the low frequency platform motion. The CPS signal in this case becomes:

$$x_{\text{CPS}} = F_{LP} (x_p - x_g) + F_{SC} x_g \quad (1.29)$$

where  $F_{SC}$  is the “sensor correction” filter which has a pass band which overlaps the CPS low pass filter. This can be rearranged to give:

$$x_{CPS} = \tilde{F}_{LP} (x_p - x_g) + \tilde{F}_{HP} x_p \quad (1.30)$$

where the tildes denote the relevant combination of  $F_{LP}$  and  $F_{SC}$ . This scheme allows for isolation down to **10 mHz** and decreases the bleed through of ground motion due to the CPS low-pass filter’s finite roll off. Below 10 mHz, both the ground and platform seismometers become dominated by tilt contamination which is addressed in the following Section 2.1.

## Chapter 2

### 1-M SCALE GROUND ROTATION SENSORS

#### 2.1 *Tilt Contamination*

At their core seismometers are low frequency spring mass system which measures the difference in motion between the casing and the device's proof mass. Above the resonant frequency of the spring mass system, this allows for accurate measurements of the motion in reference to an inertial frame of any object that the casing is rigidly connected to, be it the ground or a suspended table. Over the past **some time** this technology has produced devices that are sensitive to **number and range**. However, these systems are fundamentally susceptible to any stray forces acting on the proof mass.

Of interest here is the contamination due to the rotation of the device within a external gravitational field, namely the field caused by the earth. The rotation in respect to a fixed gravitational force will be referred to as tilt.<sup>1</sup> From the proof mass's frame, a tilt is equivalent to a rotation of the gravitational force. This yields a horizontal acceleration of the proof mass of:

$$a = g \sin(\theta)$$

where  $g$  is the gravitational acceleration on the surface of the earth and  $\theta$  is the angle that the device is rotated. This acceleration adds a second term to the seismometer's output shown below for small angles and in the Fourier domain:

$$\tilde{x}_{seis}(\omega) = \tilde{x}_{trans}(\omega) + \frac{g}{\omega^2} \tilde{\theta}_{wind}(\omega)$$

---

<sup>1</sup>Although a subtle difference, the distinction would be of great consequences if the local gravitational field was varying rapidly. In that case the sensors described here would be of little use as they are rotational sensors not tilt sensors.

where  $x_{seis}$  is the seismometer's output,  $x_{trans}$  is the translational motion of the device, and  $\omega$  is the frequency at which the tilt is being driven.

With this additional contribution, it becomes immediately clear that, for a given amplitude of tilt, the contamination term contributes more at lower frequencies and readily dominates the translational signal. In the context of the ground seismometers at the observatory, the tilt signal swamps the translational component below  $\sim 100$  mHz. Above which the seismometer signal is dominated by the ever present oceanic microseism which is driven by low frequency pressure waves with the ocean and their interaction with the shoreline. **CITE** This can be seen in Figure 2.1 which shows an amplitude spectral density of a ground seismometer at LHO during both low and high wind conditions.

The dominant driver of ground tilts at the observatories is wind acting on the walls of the building. Although one would naively assume that the wind would rigidly rotate the building, it was found that the true mechanism is differential pressure acting on the walls deforms the building's concrete slab. **cite?**

## ***2.2 Sensor Correction with Tilt Subtraction***

There are a few different ways to combat such a contamination. The most straight forward is to decrease the wind pressure by designing builds that don't interact with the wind as much or installing wind blocks such as wind fences or earth berms. Both of these options require significant construction and for the case of LIGO, tilt contamination was not known to be a problem when designing the observatories. Another option is to build seismometers that are suspended in such a way that they do not experience tilts. This is an active area of research and may yield tilt-free seismometers. **cite**

The scheme that will be used here is to measure the tilt with an independent rotation sensor and subtract the wind driven contribution. This would then yield a channel of the

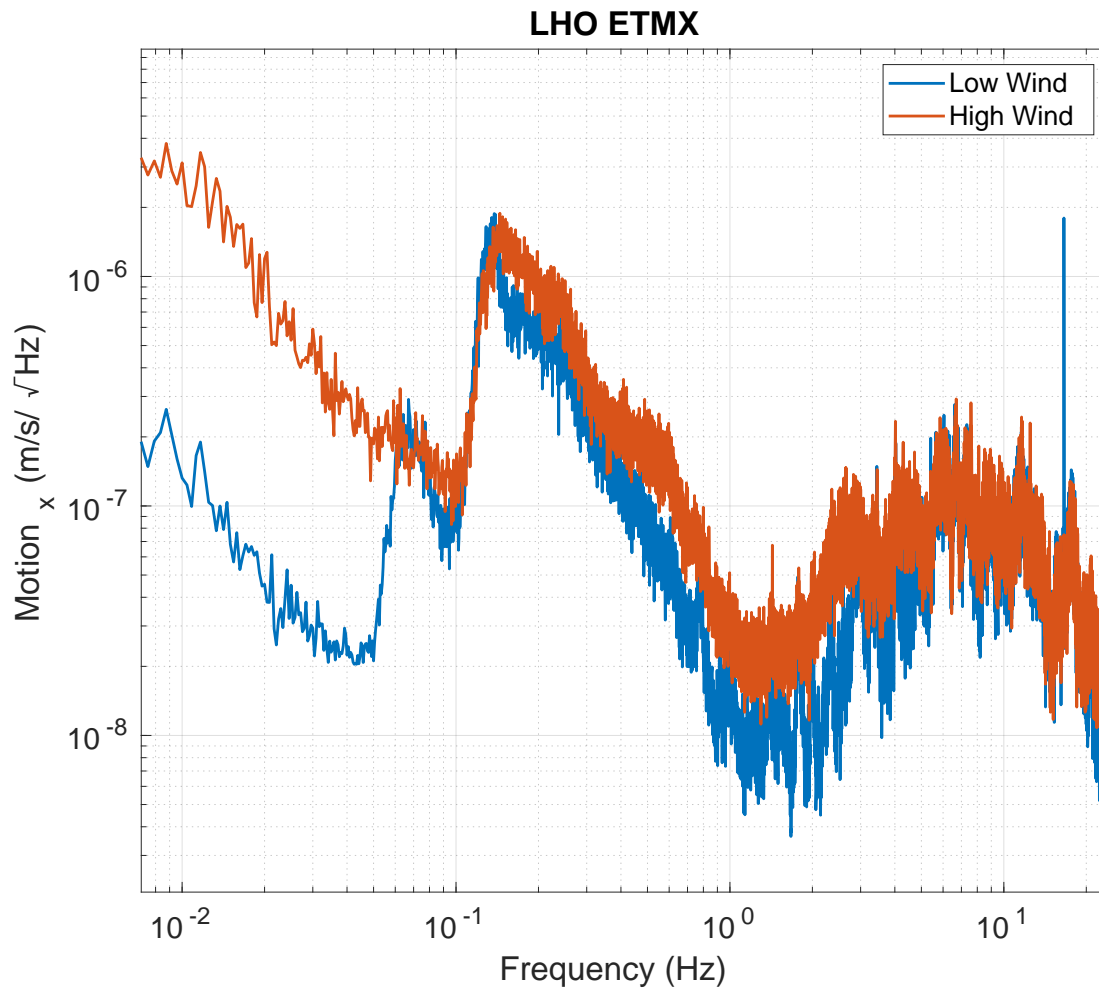


Figure 2.1: Ground motion spectra recorded at the X end station of the Hanford Observatory during low and high winds. Below 100 mHz, wind driven tilts become dominate during high winds. From 100 mHz to 1 Hz the spectra are dominated by the oceanic microseism while above 1 Hz the seismic motion is sourced by local athropogenic activity.

following form:

$$x_{seis}(\omega) = x_{trans}(\omega) + \frac{g}{\omega^2} \theta_{wind}(\omega) \quad (2.1)$$

$$- \frac{g}{\omega^2} \theta_{meas}(\omega) \quad (2.2)$$

where  $\theta_{meas}$  is the tilt seen by the rotation sensor. Given a coherence  $\gamma$  between the tilt component of the seismometer and rotation sensors this yields the following: **CHECK math**

$$x_{seis}(\omega) = x_{trans}(\omega) + \frac{g}{\omega^2} (1 - \gamma) \theta_{wind}(\omega)$$

This is then a low tilt channel which can be used within the LIGO seismic isolation system.

### 2.3 Mechanical System

The Beam Rotation Sensor (BRS) is a beam balance comprised of a 1-m long beam hung from two 10-15  $\mu\text{m}$  thick beryllium-copper flexures. Figure ?? shows a CAD model of the beam balance.

This design makes the beam stiff in all degrees of freedom other than rotations around the horizontal axis which intersects the two flexure pivot points. This forms a system consisting of two elementary subsystems: a rotational spring mass system formed by the stiffness of the flexures, and a simple pendulum due to the offset of the pivot point and the center of mass. This is then described by the following equation of motion: [19]

$$I\ddot{\theta}(t) + \kappa(1 + \frac{i}{Q})(\theta(t) - \theta_p(t)) + Mg\delta\theta(t) + M\delta\ddot{x}_p(t) = \tau_{ext}(t)$$

where  $\theta$  and  $\theta_p$  are, respectively, the angle of beam and the platform with respect to gravitational vertical,  $\tau_{ext}$  is the sum of all exterior torques,  $I$  is the moment of inertia,  $Q$  is the quality factor of the system,  $\kappa$  is the spring constant of the flexures,  $M$  is the mass of

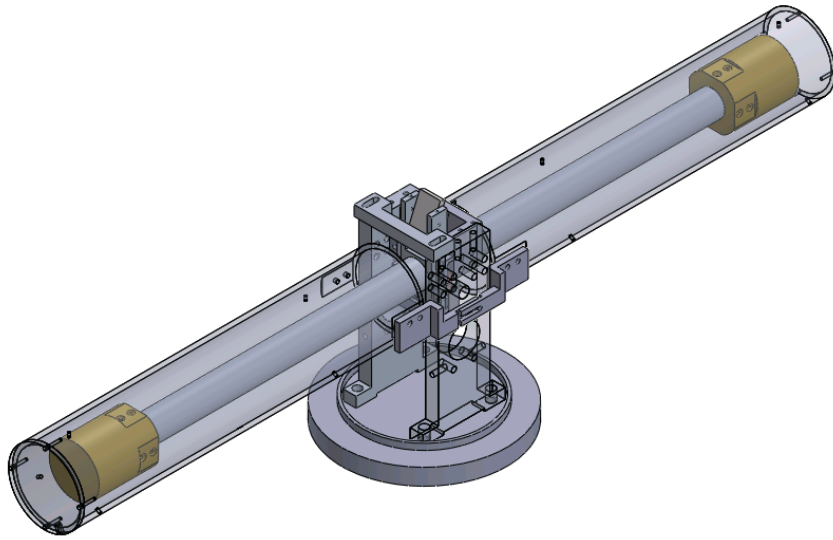
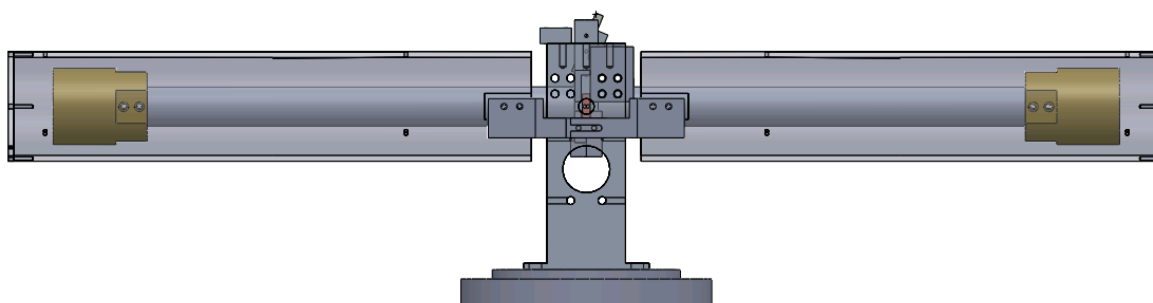


Figure 2.2: CAD rendering of the Beam Rotation Sensor with the vacuum and optical readout systems omitted. The beam with its two brass end masses can be seen through the thermal shielding, shown here as transparent.





the balance,  $g$  is the gravitational acceleration,  $\delta$  is the vertical distance from the center of mass and the pivot point, and  $x_p$  is the translation of the platform.

### **derive translational coupling and readout equation**

In ideal operation, one would tune the center of mass to be at the pivot point and thus would produce a pure rotational spring-mass system with no translational coupling. In this limit, the rotation sensor is a rotational analog to a seismometer; above the resonant frequency as the casing rotates the beam stays inertial and thus allows one to measure the casing's rotation.

## **2.4 Multi-Slit Autocollimator Readout**

Optical levers are a simple optical angular readout which exploits the law of reflection to measure angular deflections of a mirror by observing the displacement of a reflected beam. The angle of the mirror is then described as:

$$\theta_{mirror} = \frac{x_{reflected}}{2d}$$

where  $\theta_{mirror}$  is the angle of the mirror,  $x_{reflected}$  is the displacement of the reflected beam, and  $d$  is the distance between the optical system and the mirror. This allows one to increase the precision of the angular measurements arbitrarily by increasing  $d$ . However, with this comes a few disadvantages. One the effective gain of the sensor depends of the  $d$  which may not be well known. Additionally, the system is sensitive to changes in  $d$ .

An autocollimator adds a lens located one focal length from light source and the screen, shown in Figure **number**. This effectively replace the distance dependence with the focal length of the lens which allows the system to be only sensitive, to first order, to the angular motion of the mirror.

### **autocollimator schematic**

To improve upon this further, a partially reflective mirror can be placed in between the optical system and the main mirror to act as a reference and allows for the subtraction of any

motion of the optical system with respect to the main mirror. This yield a angular readout described by:

$$\theta_{mirror} = \frac{x_{main} - x_{reference}}{2f}$$

where  $f$  is the focal length of the lens and  $x_{reference}$  is the beam spot from the reference mirror.

**make table of BRS autocollimator parameters: focus, number of slits, slit width, CCD type, light source, frequency**

An increase in sensitivity can be made by employing a multi-slit autocollimator [3]. This consists of an autocollimator with the light source replaced by a illuminated photomask of a number of thin slits. The pattern is then reflected off a set of reference and main mirror and imaged by a line CCD camera. These images are then analyzed to measure the distance between them thus yielding a measurement of angle. For the BRSs, this image analysis is achieved using bespoke software written in C# which can be found at [www.github.com/mpross/BRSReadout](http://www.github.com/mpross/BRSReadout)

To extract the distance between the patterns, the image goes through a series of steps to go from a vector of pixel intensities to a single angular output. When the software begins, the first frame that is captured is saved. All future frames are split into two, with one part representing the reference mirror and the other the main mirror. The cross correlation is then taken between each part and it's matching part from the first frame. This gives a curve who's maximum is located at the pixel number corresponding to separation between the pattern in the current frame and the first frame, which can be seen in Figure **number**. The points of this curve that are near the maximum are then fit to a Gaussian which allows for the extraction of the location of the peak with sub-pixel resolution. This is done for each pattern separately after which the difference between the reference pattern location and the main pattern location is taken. The difference is then proportional to the change in angle between the casing and the beam.

Compared to previous image analysis algorithms [? ], this algorithm is more computa-

tionally efficient while also being less susceptible to variations in the pattern image due to dust particulate, incorrect focusing, or beam clipping. A sensitivity of  $\sim 0.1 \text{ nrad}/\sqrt{\text{Hz}}$  was achieved with this autocollimator design and image analysis algorithm.

## 2.5 Controls

As the BRSs are installed in active lab spaces, anthropogenic actively and environmental disturbances regularly apply torques on the beam balance, either through mechanical coupling through the flexures or gravitational coupling with the end masses. These can then cause the motion at the resonant frequency to rise to undesirable amplitudes. As the beam motion increases so does the noise. Additionally, some disturbances can be large enough to cause the amplitude to exceed the dynamic range of the autocollimator readout system.

To alleviate this issue, capacitor plates are installed underneath each end of the beam balance to act as actuators. The force between the two capacitor plates follows the following:

$$F = \frac{\epsilon AV^2}{2d^2} \quad (2.3)$$

where  $\epsilon$  is the permittivity of the material between the plates,  $A$  is the area of the plate,  $V$  is the voltage applied to the plates, and  $d$  is the distance between the plates. The plate under the beam is connected to a DAC while the beam is grounded which allows for a controlled actuation torque to be applied to the beam.

The control scheme that was adopted was one in which the feedback signal that is sent to the capacitors is the angular velocity of the beam band passed between 2 mHz and 20 mHz to include only motion at frequencies near the resonance. The feedback is additionally applied with low gain so that the feedback is only adding loss to the system as compared to locking the system in a strong feedback loop where all of the motion is absorbed into the control system. This is then implemented with two gain stages, a “low amplitude” stage which is always on and yields a Q of 10-15 and a “high amplitude” stage which is triggered if the amplitude rises above a threshold that is set based on the behavior of the given device

and gives a Q of **number**.

## 2.6 Noise Performance

In addition to the  $0.1 \text{ nrad}/\sqrt{\text{Hz}}$  white noise of the autocollimator readout, these devices suffer from a various mechanical noise sources, namely noise due to temperature variations and due to the thermal motion of the flexures.

Although the exact physical mechanism is unknown at this juncture, it has been observed that variations in the exterior temperature cause shifts in the balance's equilibrium position. Furthermore, temperature gradients across the instrument emanating from unbalanced heat sources and air currents have been seen to cause time varying noise. To alleviate this issue the instrument's vacuum chamber and optics are wrapped in multiple alternating layers of packing foam and aluminum foil. The entire apparatus is then placed inside a large double walled insulation box to further decrease any temperature variations. This eliminates this as a dominate noise source unless the room in which the instrument is housed undergoes large temperature variations.

More limiting is the noise due to the thermal vibrations of the flexure. At any non-zero temperature, a portion of the thermal energy of the flexures is stored in the vibrational modes of the flexure. This causes a fundamental stochastic noise floor that goes as such: **add thermal noise equation** since this noise source enters as a torque on the beam balance, it is filtered by the harmonic response making it fall as  $1/f^2$  above the resonant frequency. To limit the influence on the performance of the device, the resonant frequency of the spring mass system is pushed to the lowest frequency that is mechanically feasible.

One further noise source that acts on the beam balance comes from voltage noise on the capacitive actuators. The force caused by the follows Equation 2.3 and can be shown to be sub dominate.

The noise budget for a BRS is shown in Figure 2.3 which shows that the device is readout dominated above  $\sim 20 \text{ mHz}$  and below is dominated by thermal noise. An excess in the measured noise can be seen below  $3 \text{ mHz}$  which is believed to be due to residual

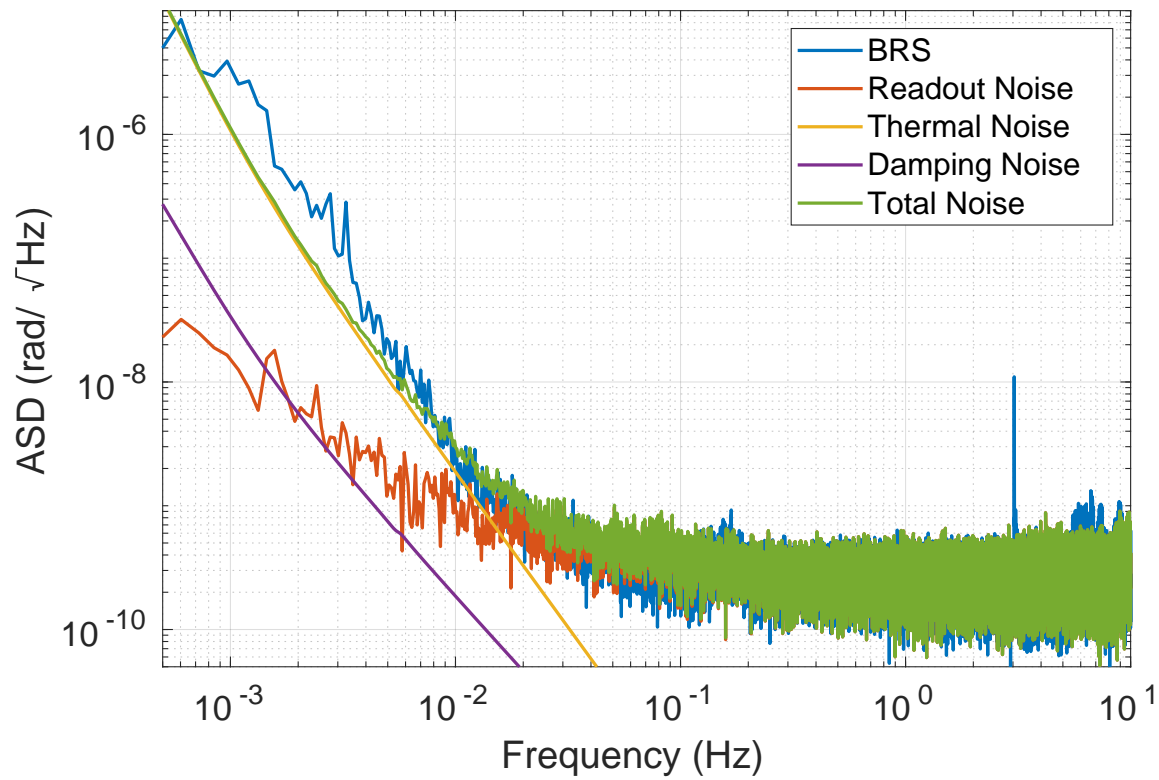


Figure 2.3: Noise budget for the Beam Rotation Sensors where the blue curve shows the performance at a quiet time, in red is the motion of the reference mirror which can be regarded as an estimate of the readout noise, yellow shows an estimate of the thermal noise, purple shows the noise from the capacitive actuators, and green shows the some of all known noise sources.

temperature noise. Respectively at 150 mHz, 3 Hz, and 6 Hz the rotational microseism, torsion mode of the beam balance, and motion due to nearby instrumentation can be seen above the predicted noise sources.

## **2.7 Hanford Installation**

Between the first (O1) and second (O2) observing runs of LIGO, two BRSs were installed at the LIGO Hanford Observatory, one at each end station correcting the translations along their respective arm. Although one would expect that the corner station sensors would also need to be corrected, a location was found within the corner station building which exhibited low tilt. **cite** This is thought to be due to the shape of the building the distance between this location and the walls. As such no BRS was necessary to achieve low tilt injection seismic isolation.

The tilt subtraction performance achieved with these devices can be seen in Figure 2.4 where it is evident that the system achieves tilt subtraction from around 6 mHz to 50 mHz. Above 50 mHz the seismometer signal is dominated by the oceanic microseism and the tilt contribution is negligible. Below 6 mHz, the BRS signal becomes overwhelmed by instrumental noise. This performance can also be seen in Figure 2.5 which shows a example time series of the tilt subtraction.

This tilt subtracted channel was then used as the ground signal for the isolation's sensor correction instead of the raw seismometer. Along with the use of the low tilt seismometer for the corner station, the addition of the BRSs in the seismic control scheme yielded significant improvements in the ability to lock the interferometer at increased wind speeds which can be seen in Figure ??

## **2.8 Livingston Installation**

After the success of the Hanford BRS installation, four devices were installed at the LIGO Livingston Observatory (LLO) between the second and third (O3) observing runs. Due to differences in the size and shape of the corner station building at LLO a low tilt location

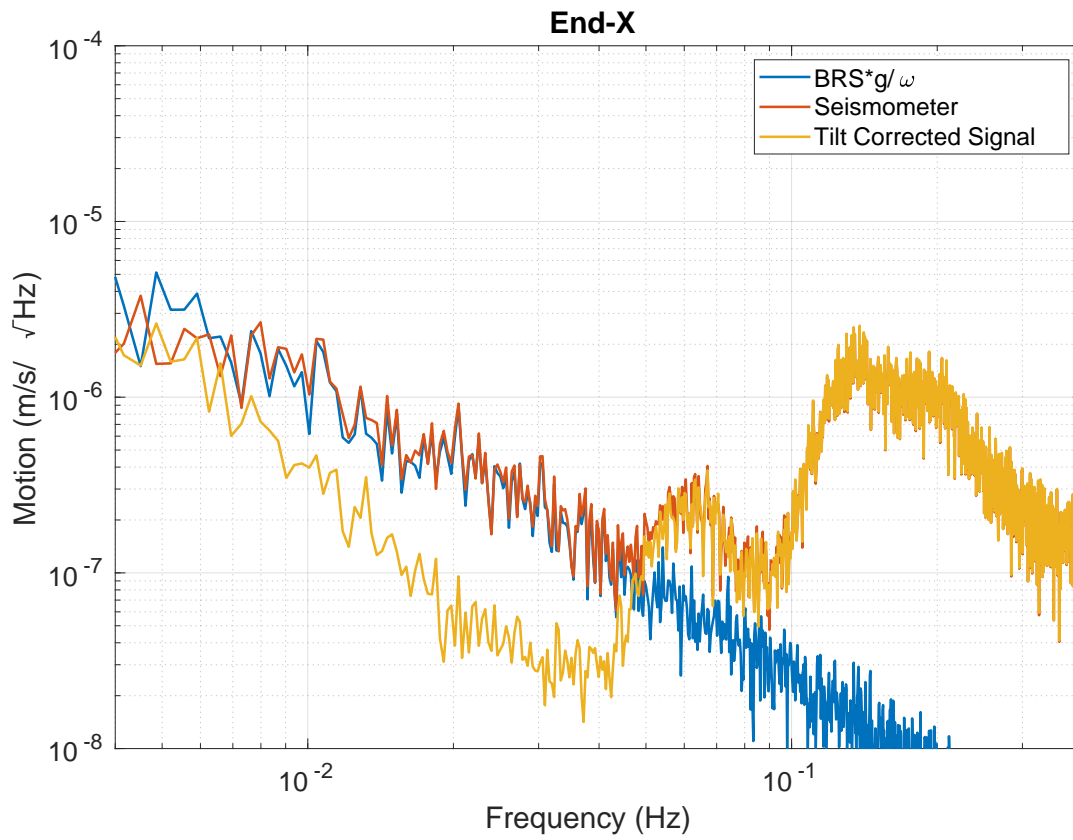


Figure 2.4: Representative amplitude spectral density showing the tilt subtraction during windy conditions achieved at End-X of LHO where blue is the BRS signal multiplied by  $g/\omega$ , red is the raw seismometer signal, and yellow is the tilt corrected signal. Similar performance has been achieved by all of the installed BRSs.



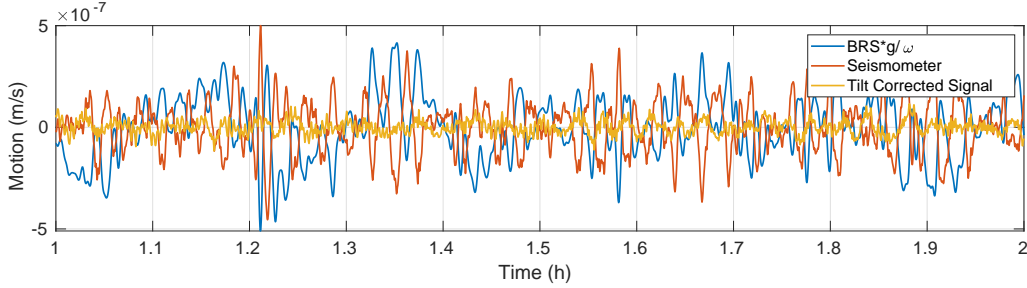


Figure 2.5: Time series showing the tilt subtraction at End-X of LHO where blue is the BRS signal multiplied by  $g/\omega$ , red is the raw seismometer signal, and yellow is the tilt corrected signal. As can be seen, the tilt subtraction removes a collection of transients, likely due to the gusts of wind.

was not found. Thus two BRSs were installed located near the two input test masses (ITM) correcting the seismometer signal oriented along their respective arms.

All four were implemented in a similar fashion as the Hanford devices.

## 2.9 Duty Cycle Improvements

The figure of merit which most readily displays the improvements in duty cycle due to inclusion of the BRSs is the empirical probability of being locked at a given wind speed over the three observing runs. This is shown in Figures 2.6 and 2.7 for LHO and LLO, respectively. It should be noted that BRSs were implemented in the isolation system at Hanford for both O2 and O3a while Livingston was only for O3a.

For Hanford, the benefit of the tilt subtraction scheme can clearly be seen between O1 and O2 curves. During O1 the locked probability fell monotonically with wind speed, while for O2 the probability stayed relatively constant up to 15 m/s above which it fell steadily. For O3a, Hanford saw a clear decrease in performance at high wind speeds yet still out performed the O1 scheme. This loss of performance is likely due to the **Y-arm** beam being displaced away from the center of the test masses to avoid point absorbers on the **Input-Y** test mass. This is known to increase coupling between the angular motion of the test mass and the

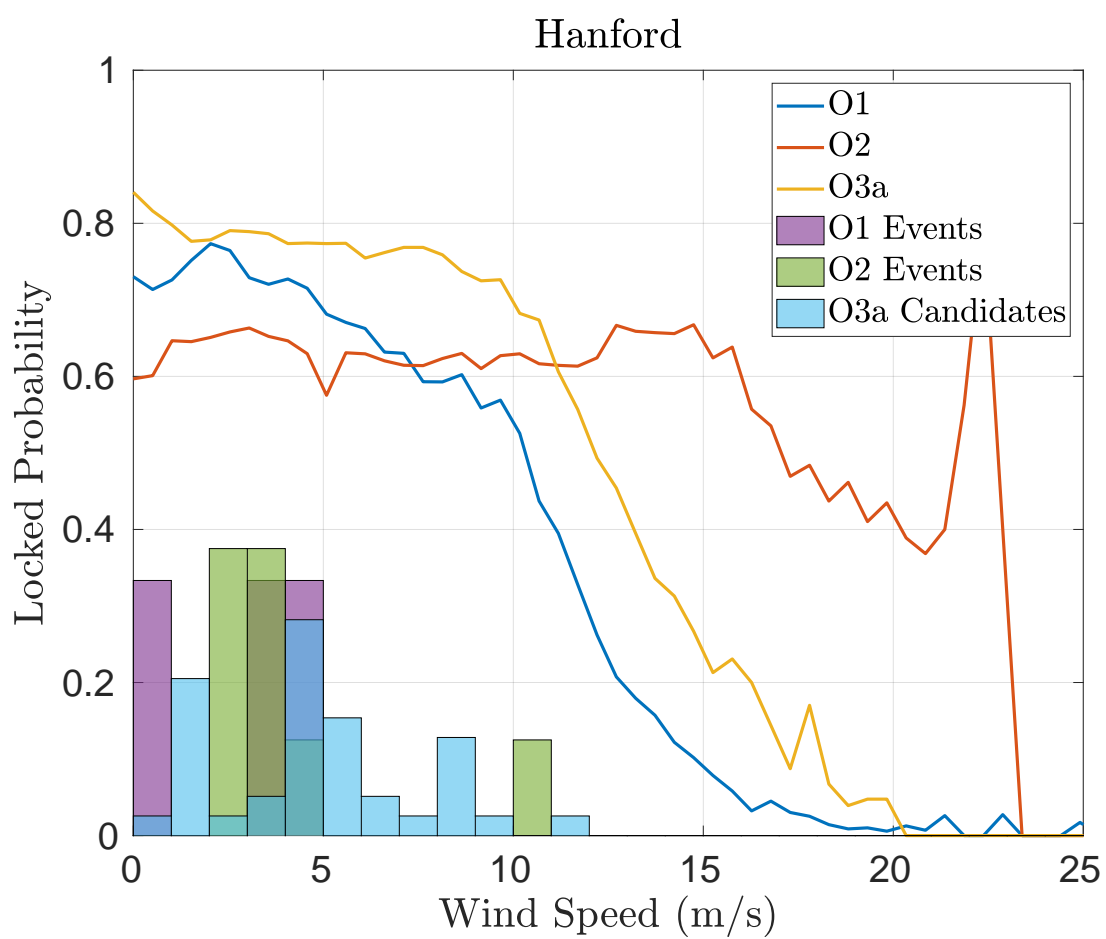


Figure 2.6

length measured by the interferometer and thus decreases the seismic isolation performance.

Also shown in Figure 2.6 is the fraction of the GW events detected during O2 and the fraction of O3a GW candidates at a given wind speed. This shows that a collection of GW events have been observed whose detection probability is directly increased due to the increase duty cycle at higher wind speeds. Namely, GW170104 was measured at **11 m/s** which had an increase in duty cycle of **20 %** between O1 and O2. Additionally, a number of O3a candidates have been detected above **5 m/s** at which the probability of being locked is increased by **20 %**.

At Livingston, the improvements at increased wind speeds is less dramatic as can be seen in Figure 2.7. Although between O1 and O2 tilt subtraction was not implemented, a increase in duty cycle was achieved by using a single seismometer for the sensors correction on all of the corner station chambers. This decreased the differential mode motion at higher wind speeds and thus made the interferometer lock more robust. An addition increase in performance can be seen between O2 and O3a due to the deployment of tilt subtraction. However, the probability of being locked still dropped monotonically with wind speed, similar to the O1 performance of Hanford.

Despite this, there is still a collection of O3a candidates detected between **3-6 m/s** which are more probable with the increased robustness against wind speed.

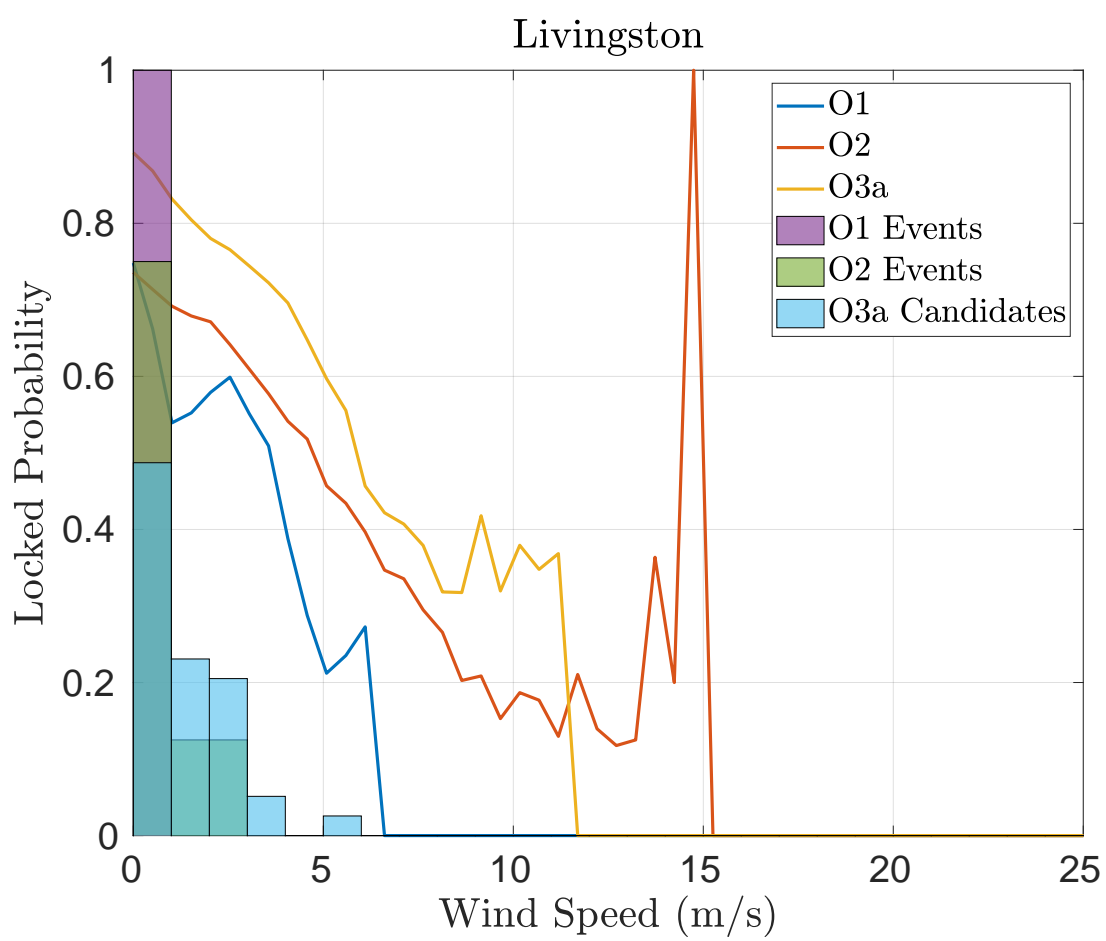


Figure 2.7

## Chapter 3

### 30-CM SCALE ON-BOARD ROTATION SENSORS

#### 3.1 *Angular Controls*

To operate the LIGO interferometers in their optimal configuration, the angular motion of the test masses in the pitch degree of freedom must be under **number** nrad/ $\sqrt{\text{Hz}}$  at **number** Hz where as the ground rotates at  $\sim$ **number** nrad/ $\sqrt{\text{Hz}}$  at **number** Hz. To achieve this desired performance, the seismic isolation operated in the rotational degrees of freedom as well as the translation. Additionally, the upper three masses of the quadruple pendulum are actively actuated at frequencies between **number** and **number** Hz to decrease any residual motion.

With the current system, at **number** Hz the seismic isolation is limited by the sensor noise in the seismometer pair which forms the pitch sensor. This then requires high gain feedback loops on the angular control loop downstream, which themselves are limited by their respective sensor noise at **number** Hz. This left over noise then leaks into the gravitational wave band between **number** and **number** Hz due to the inability to sharply roll off the control without interfering with control at lower frequencies.

The compact Beam Rotation Sensor (cBRS), described in the following, was designed to be an alternative angular sensor for the seismic isolation system with **number** times lower noise than the current sensors. With this decreased noise, the seismic isolation control loops can be tuned to significantly increase the performance of both the translational isolation, through decreased tilt contamination described in Section ??, and directly the rotational isolation. Details of this follow in Section 3.2. This decreased residual rotation would then allow the angular control loops to be retuned, specifically decreasing the gain, to push the sensor noise leakage below the design sensitivity. **Need to check this.**

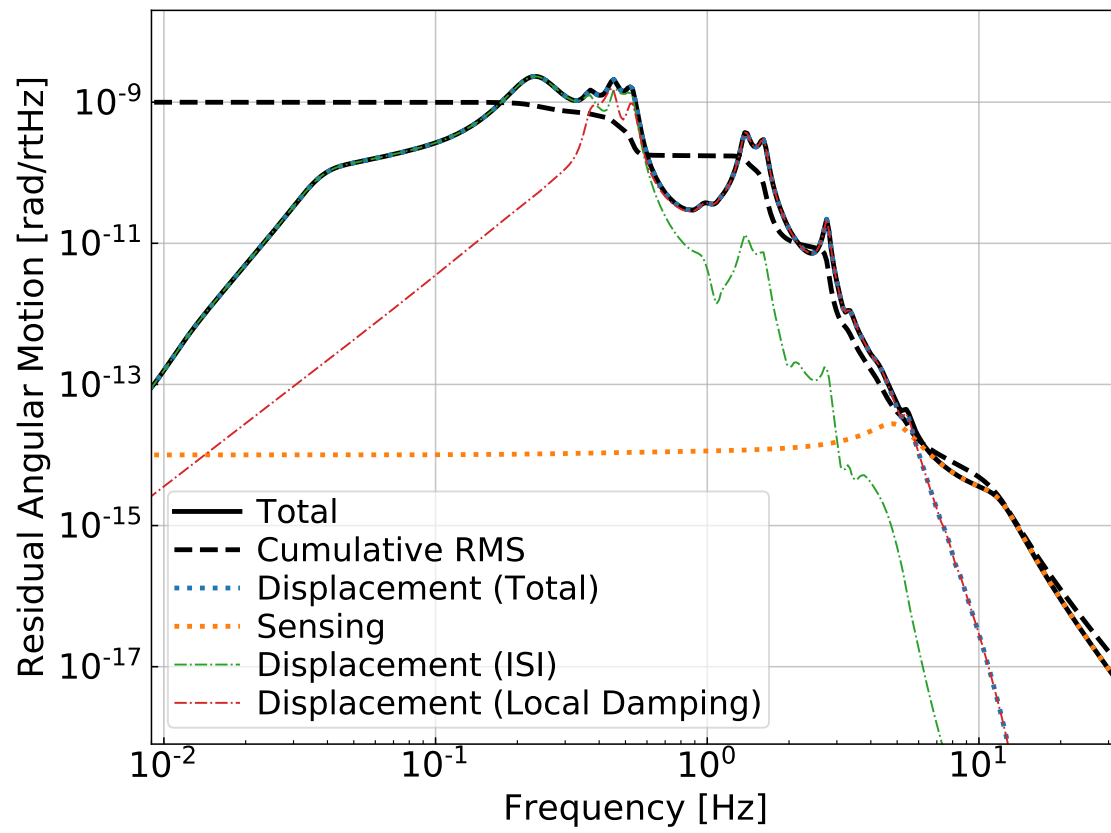


Figure 3.1: Performance of the current angular sensing and control system.

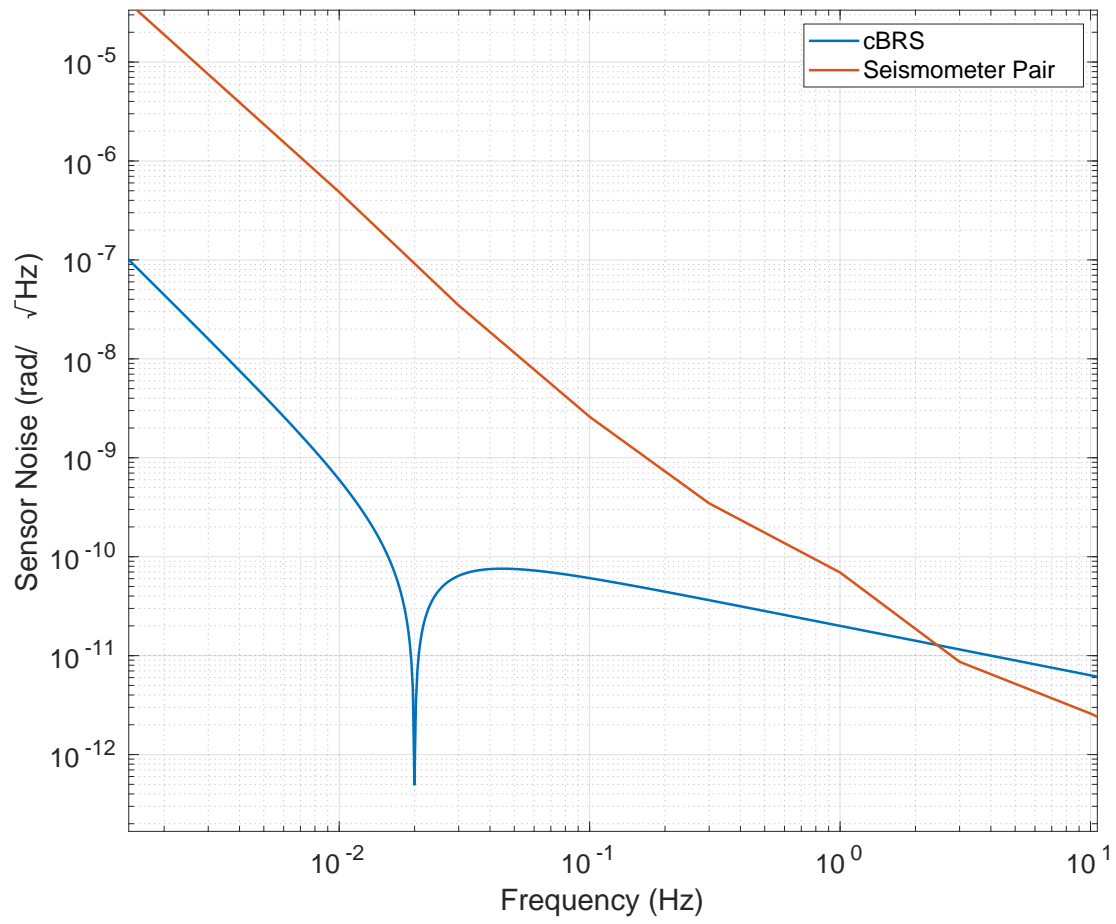


Figure 3.2: Theoretical noise curves for the cBRS, blue, and seismometer pair located 1-m apart.

### **3.2 Isolation Scheme**

Assuming that the isolation is limited by the noise of the in-band sensor, placing the lowest noise sensors on the second stage of the ISI would be expected to yield the lowest angular motion seen by the down stream control loops. With this in mind and the fact that the access to place new sensors is easier for the second stage, a control scheme was modeled which consists of the addition of an idealized cBRS (described in Section ??) on stage 2. This model consisted of only two mechanical degrees of freedom, one horizontal translation and the rotational about the orthogonal horizontal axis.

The rotational control loop for stage 2 then consists of using the CPS between stage 1 and stage 2 at low frequencies, the cBRS at frequencies between 3 mHz and 0.9 Hz, and the GS-13 pairs at frequencies above that. The blend frequencies were tuned to minimized the rms motion at low frequencies while maximizing the isolation at 0.1 Hz.

### **3.3 Projected Angular Control Improvements**

#### **3.4 Mechanical System**

Similar to the BRS described in Chapter 2, the compact Beam Rotation Sensor (cBRS), shown in Figure 3.8, consists of a 30-cm long cross hung from 10-15  $\mu\text{m}$  thick beryllium-copper flexures and has an identical operating principle as the BRS. The cross shape of the balance decreases the sensitivity of the device to gradients in the local gravitational field while allowing for increased moment of inertia compared to a similarly sized beam.

This design yields a resonant frequency of  $\sim 20$  mHz limited the use of such a device to frequencies above this.

#### **3.5 Interferometric Readout**

In order to maintain the small size of the entire device, an interferometric readout was developed that consists of a Fabry-Perot cavity that is formed by a beamsplitter coated optical fiber and the full reflectance mirror placed on the bottom of the balance's end masses.



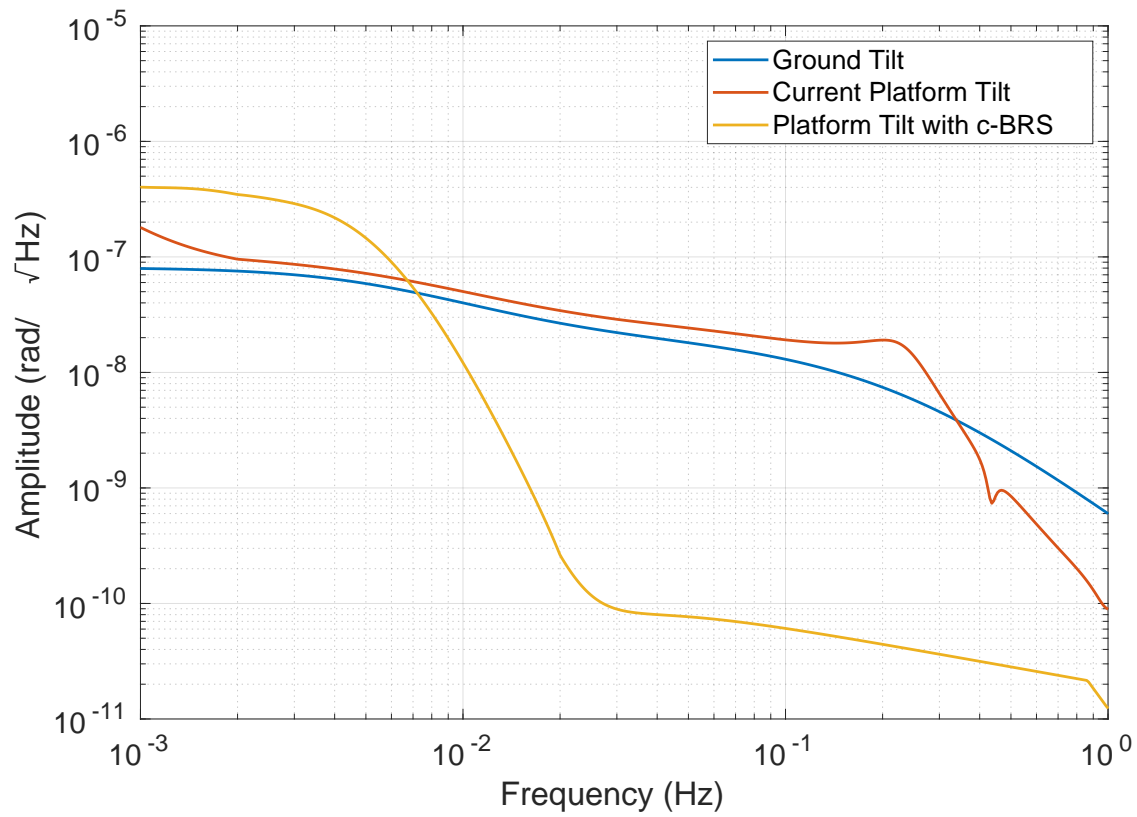


Figure 3.3: Projected rotational performance of Stage 2 of the ISI with, yellow, and without, red, the cBRS. Also shown is the input ground tilt model, blue, which represents the observed tilt during windy times.

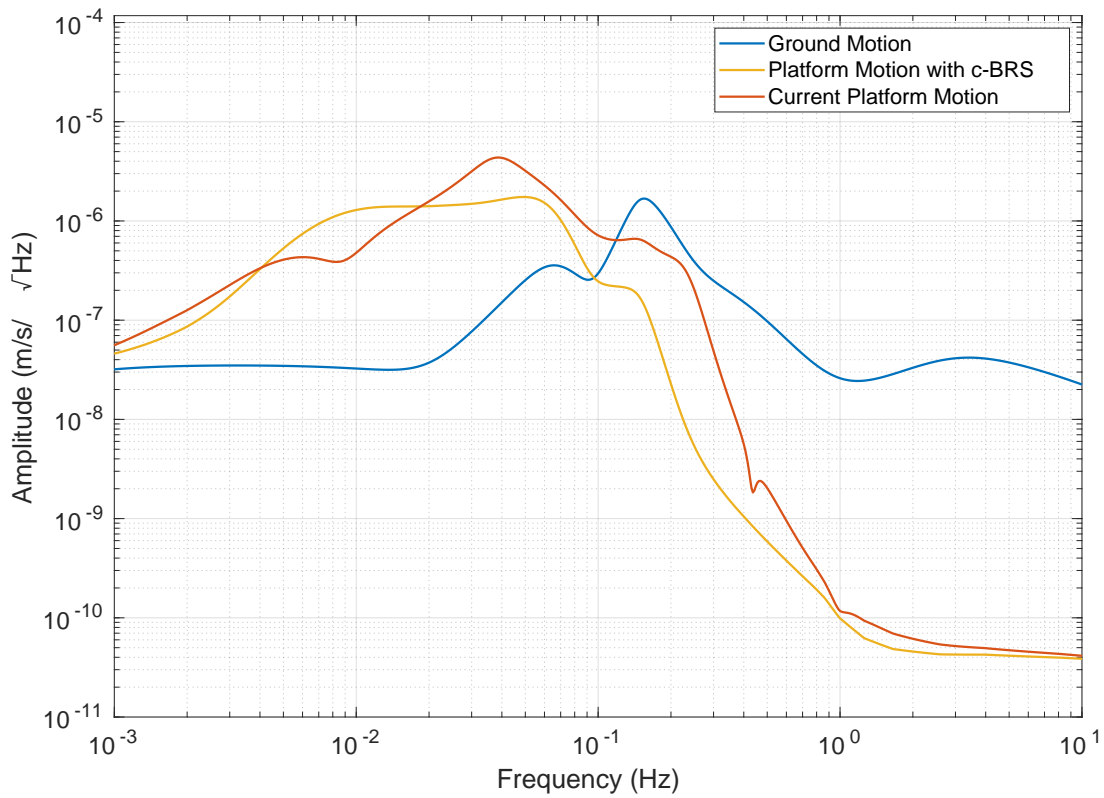


Figure 3.4: Projected translational performance of Stage 2 of the ISI with, yellow, and without, red, the cBRS. Also shown is the input ground motion model, blue, which represents the observed tilt during windy times. The control loops here can be tuned to decrease motion at  $\sim 100$  mHz, the microseism frequencies, by increasing motion at  $\sim 10$  mHz and vice versa.

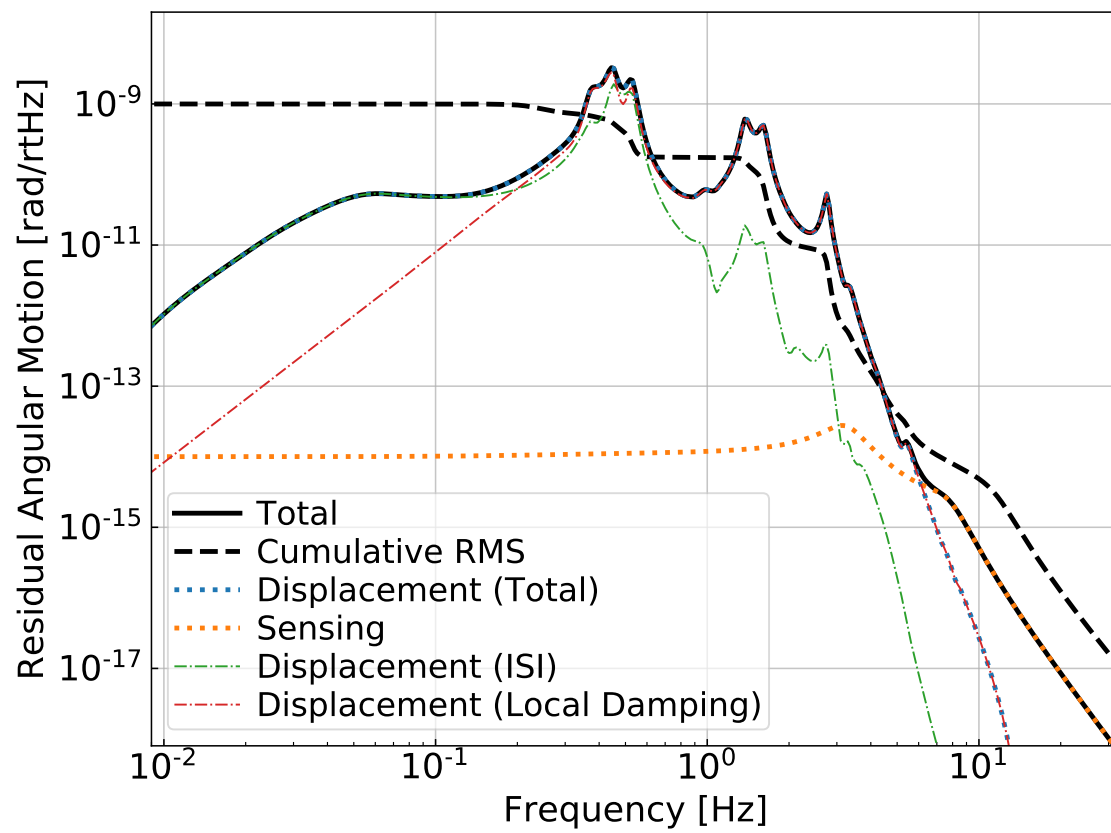


Figure 3.5: Projected performance of the angular sensing and control system with the seismic performance described in Section 3.2.

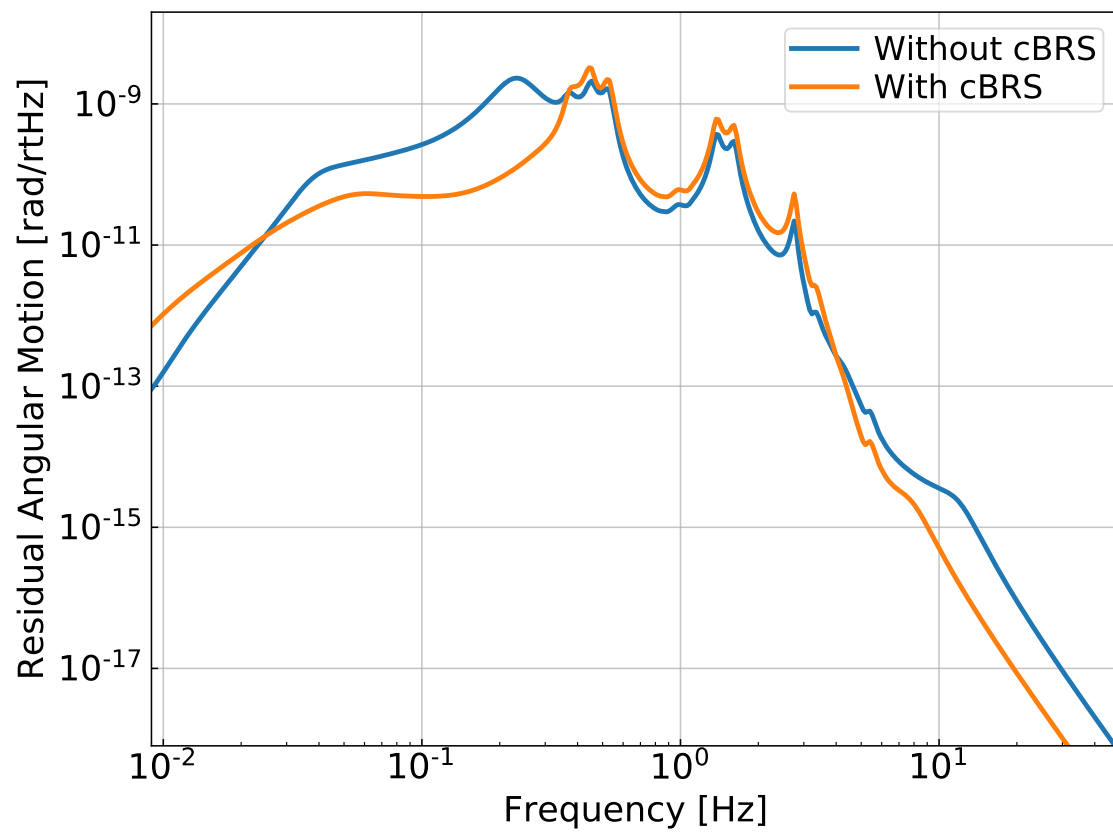


Figure 3.6: Projected performance of the angular sensing and control system with the seismic performance described in Section 3.2.

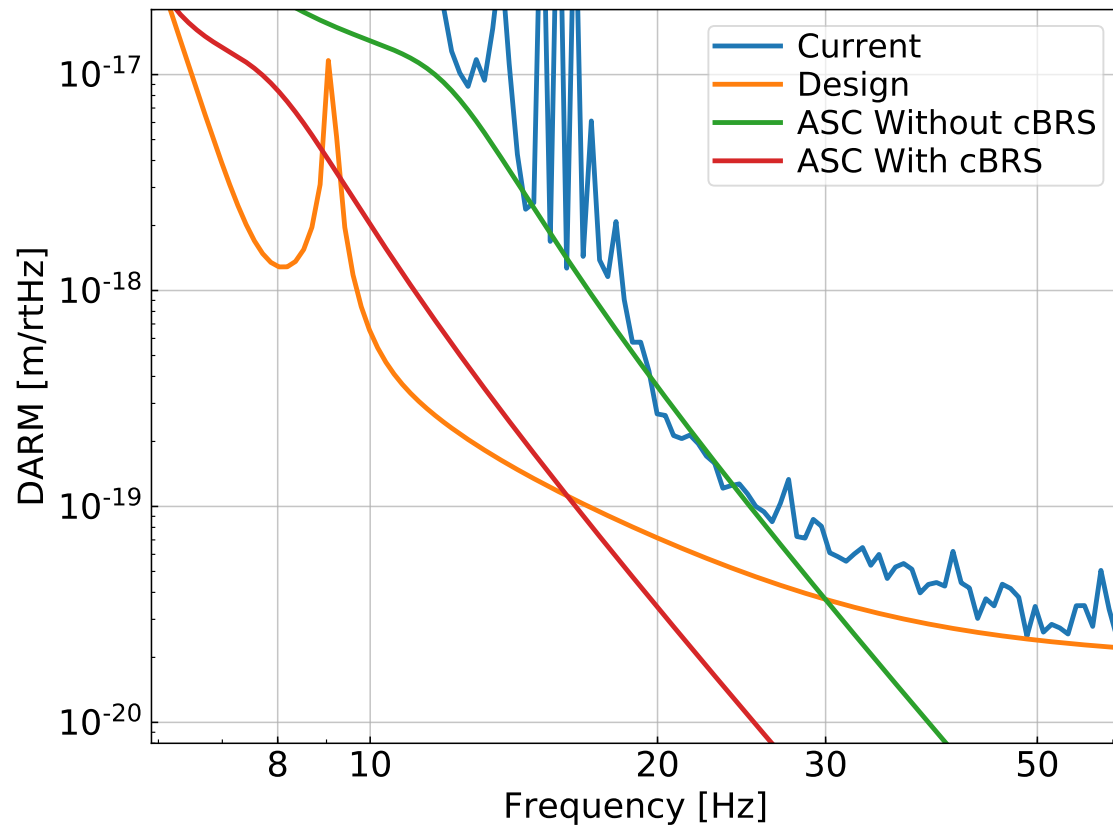
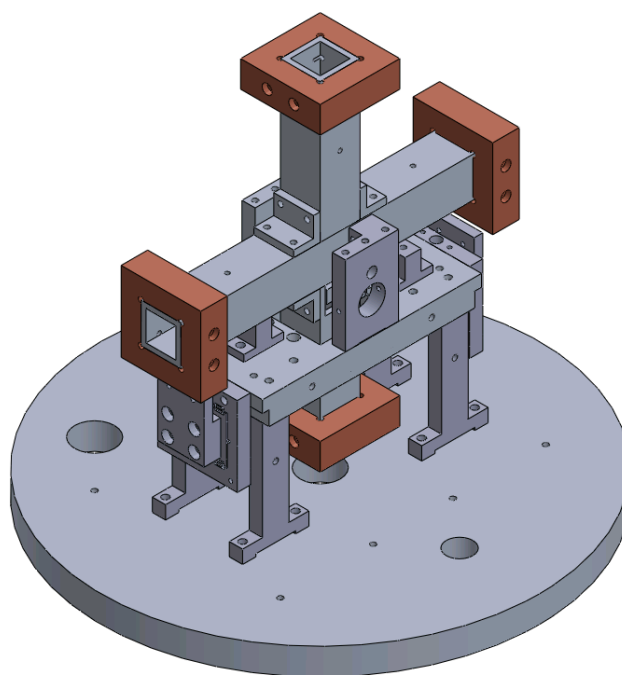


Figure 3.7: Projected low frequency strain noise with and without the cBRS. The blue line is the current sensitivity of LLO, the orange is the aLIGO design sensitivity, green is the modeled noise contribution of the current ASC system, and red is the improved ASC noise contribution with the seismic isolation described in Section 3.2.



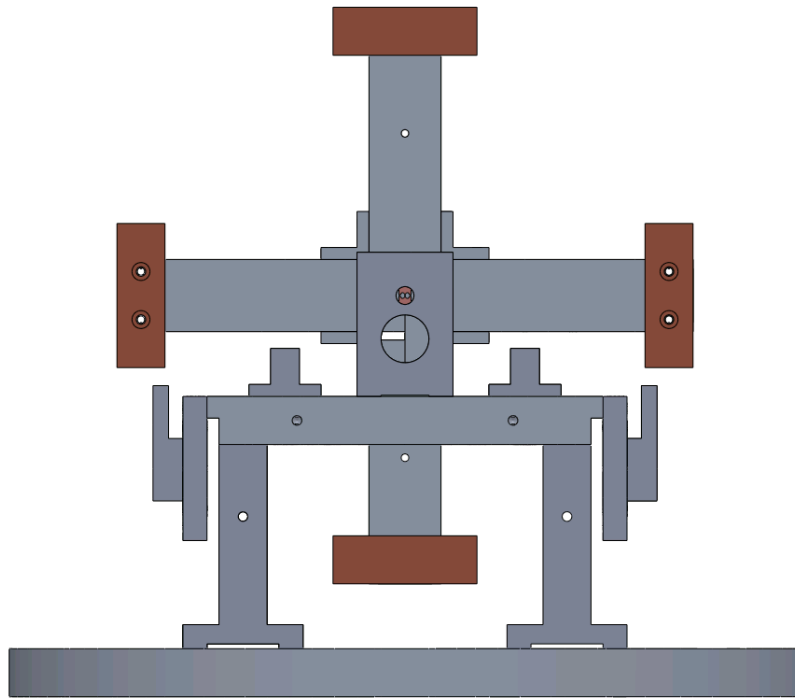


Figure 3.8: CAD rendering of the compact BRS (cBRS) showing the cross with its copper end masses which is hung from the flexures from the surrounding support structure. Additionally, the translation stages which hold the fiber interferometer readouts can be seen on either end of the support below the two horizontal end masses.

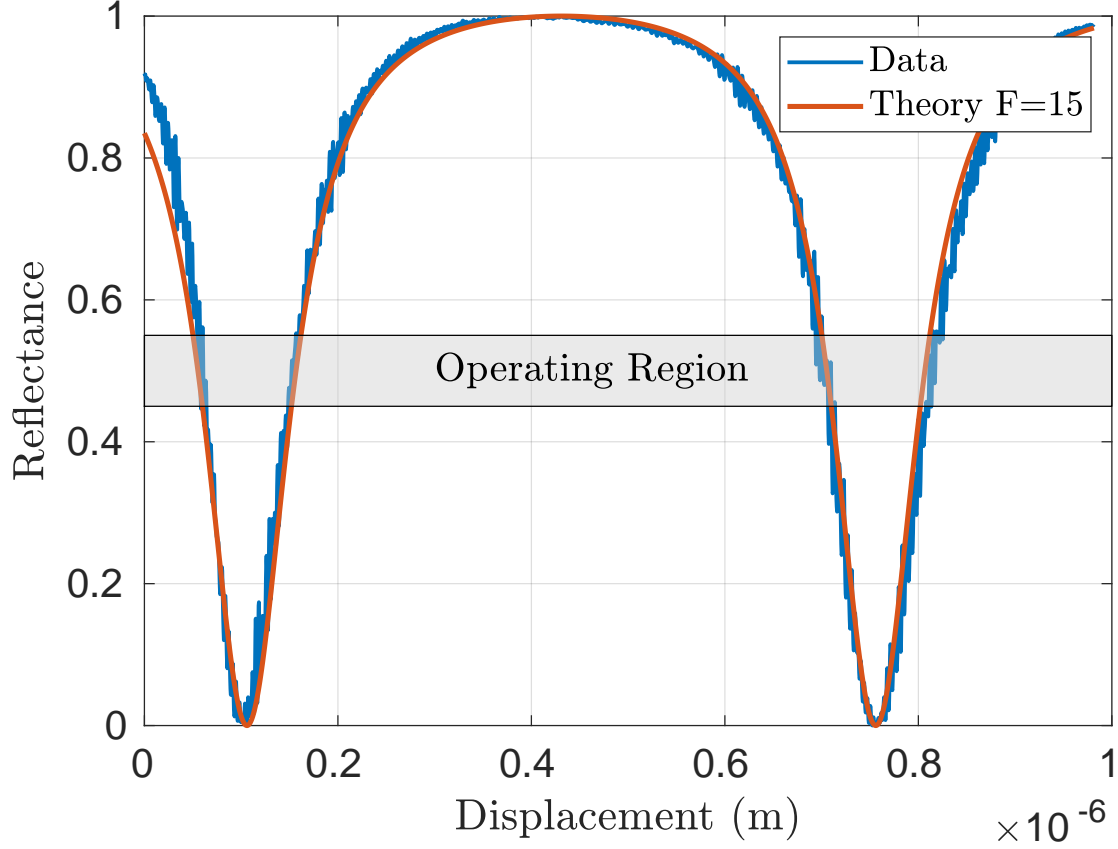


Figure 3.9

The reflectance of this cavity is then monitored by employing a circulator to separate the incoming and outgoing rays. As the cavity length changes the reflectance undergoes an interference pattern described by:

$$R = \frac{1}{1 + F \sin^2(\delta/2\lambda)} \quad (3.1)$$

#### include layout of cBRS optics

To linearize this readout, the optical fiber tip and collimating lens are placed on a translation stage that is driven by a piezo stack. The intensity of the reflected light is then fed



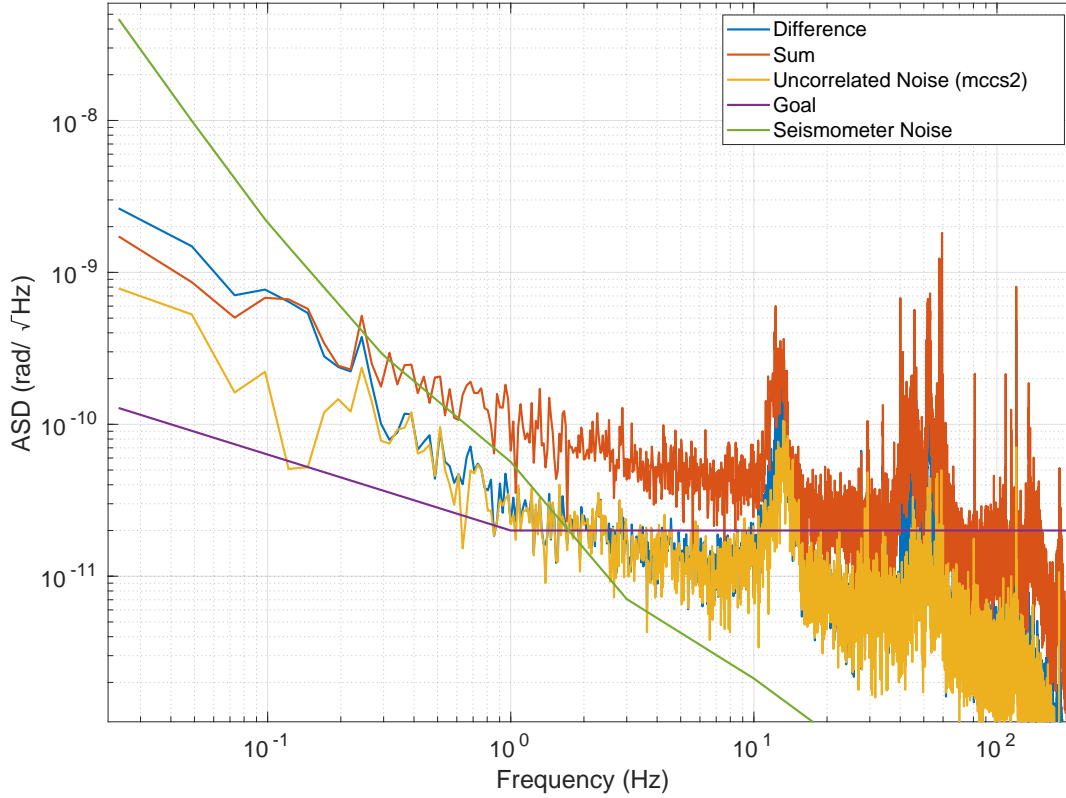


Figure 3.10

back to the piezos using a PID loop to hold the cavity length fixed. This allows the system to be separated into two linear readouts, the interferometer output for small ranges above the unity gain frequency (UGF) of the loop and the control loop output for large motions below the UGF. The output of the device is then the sum of these two channels.

**include table of PID parameters**

### 3.6 Mass Adjustment

Through a variety of mechanisms, the devices described here can undergo long term drifts of the equilibrium position that can drive the beam balance past the dynamic range of the

readout. To counteract this, a mass on the balance can be moved or added to shift the center of mass as such:

$$\Delta\theta = \frac{g}{\kappa}mr \quad (3.2)$$

where  $\Delta\theta$  is the change in equilibrium angle,  $g$  is the gravitational acceleration,  $\kappa$  is the spring constant of the flexure,  $m$  is the mass added, and  $r$  is the distance from the mass and the pivot point.

While for the BRS the horizontal center of mass (COM) was designed to be tuned by hand, for the cBRS to operate in vacuum this must be done remotely and in an automated fashion. To achieve this a mass adjuster shown in Figure ?? consisting of a small aluminum mass on a fine pitched threaded rod is placed on the beam balance.

### **3.7 Controls**

Similar to the BRS controls, the cBRS can be rung up do to environmental transients which can cause resonant motion in excess of the readout's dynamic range. To decrease these amplitudes, two capacitive actuators are placed under the end masses of the beam. These are actuated with low gain with the angular readout band passed around the resonant frequency.

### **3.8 Noise Performance**

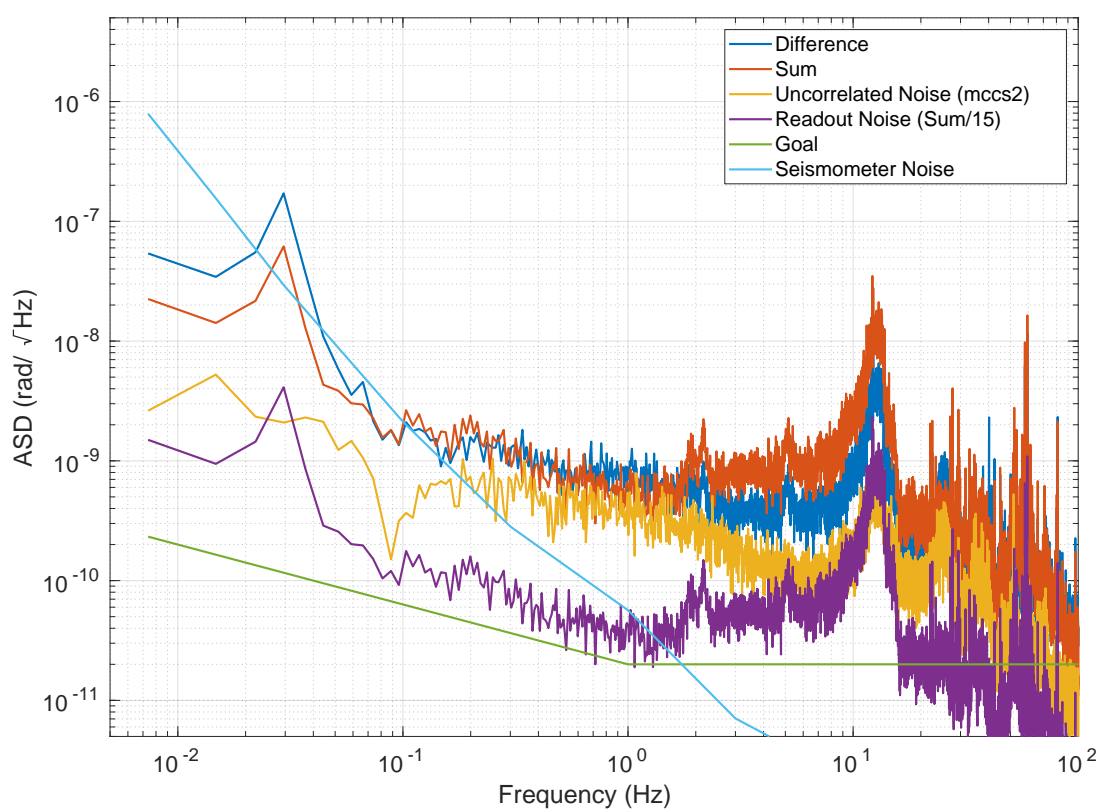


Figure 3.11

## Chapter 4

### APPLICATIONS

The development of these highly sensitive rotation sensors have opened up a few novel scientific avenues that have been explored and many that have not.

#### 4.1 *Geophysics*

Seismic waves have six components, three translations and three rotations, however seismology has long neglected the rotational components due the lack of sensitive rotation sensors. Recent developments have begun to alleviated this issue with the advent of seismically relevant ring laser gyros. **cite Gryo** The BRSs described above join a small class of ground rotation sensors with high enough sensitivity at low frequency to allow for the use in seismology.

##### 4.1.1 *Rayleigh Wave Theory*

Seismic waves can be broken into two classes: body waves and surface waves. In regard to surface waves there are two polarization, of the motion caused by a Love wave is constrained to the plane parallel with the surface of the medium while Rayleigh waves are constrained to a plane perpendicular the surface.

The plane wave solution of a Rayleigh wave has six components  $(u_x, u_y, u_z, \theta_x, \theta_y, \theta_z)$  where  $u_i$  designated the translational motion in the  $i$ th direction while  $\theta_i$  is the rotation

about the  $i$ th axis. These can be described as with the following **cite seismic paper**

$$u_x(\mathbf{r}, t) = \alpha \sin(\zeta) \cos(\psi) \cos(\omega t - \mathbf{k} \cdot \mathbf{r}) \quad (4.1)$$

$$u_y(\mathbf{r}, t) = \alpha \sin(\zeta) \sin(\psi) \cos(\omega t - \mathbf{k} \cdot \mathbf{r}) \quad (4.2)$$

$$u_z(\mathbf{r}, t) = \alpha \cos(\zeta) \cos(\omega t - \mathbf{k} \cdot \mathbf{r} + \pi/2) \quad (4.3)$$

$$\theta_x(\mathbf{r}, t) = \frac{\partial u_z}{\partial y} = \alpha \kappa \cos(\zeta) \sin(\psi) \cos(\omega t - \mathbf{k} \cdot \mathbf{r}) \quad (4.4)$$

$$\theta_y(\mathbf{r}, t) = -\frac{\partial u_z}{\partial x} = -\alpha \kappa \cos(\zeta) \cos(\psi) \cos(\omega t - \mathbf{k} \cdot \mathbf{r}) \quad (4.5)$$

$$\theta_z(\mathbf{r}, t) = \frac{1}{2} \left( \frac{\partial u_y}{\partial x} - \frac{\partial u_x}{\partial y} \right) = 0 \quad (4.6)$$

where  $\alpha$  is the amplitude,  $\zeta$  is the ellipticity angle,  $\psi$  is the angle of incidence in the horizontal plane,  $\omega$  is the frequency, and  $\mathbf{k} = \kappa(\cos(\psi), \sin(\psi), 0)$  is the wavevector.

From these equations it can be seen that with a single seismic station with a traditional 3-axis seismometer, one can not measure all five parameters that define this wave field. Additionally, the horizontal components,  $u_x$  and  $u_y$  can contain contributions from co-propagating Love waves which further muddles ones ability to extract parameters.

### **Include Earthquake plot**

#### *4.1.2 Wave Field Parameter Extraction*

With the combined measurements of the translational and rotational components at a single station, one can readily extract wavefield parameters that would otherwise be difficult to obtain, namely the phase velocity and the angle of incidence.

Seismic wave phase velocities are common observable which not only allows for understanding of Rayleigh wave propagation but can be inverted to yield tomographical structure profiles of the interior of the earth. **cite** The traditional method of extracting these is the exploit the time of arrival of a wave as it passes through an array of many seismometers. The analysis can be constrained to only the vertical channel which is insensitive to Love waves

which could contaminate the measurements. However, this method requires many devices and effectively averages over the size of the array.

Alternatively, with measurements of the rotational components a point like measurement of the phase velocity can be made with three devices, a 3-component seismometer and two horizontal rotation sensors. This can be shown in the following equations:

$$v = \frac{\omega}{\kappa} = \frac{\dot{u}_z}{\theta_x} \sin(\psi) \quad (4.7)$$

$$v = \frac{\dot{u}_z}{\theta_y} \cos(\psi) \quad (4.8)$$

$$v = \frac{\dot{u}_z}{\sqrt{\theta_x^2 + \theta_y^2}} \quad (4.9)$$

where the dot represents the temporal derivative. Equations 4.7 and 4.8 can be utilized if a station has only one horizontal rotation sensor but requires independent determination of  $\psi$ . In contrast, Equation 4.9 contains only information from a single station.

In addition to the phase velocity, the angle of incidence can be determined with the following:

$$\psi = \arctan\left(\frac{\theta_x}{\theta_y}\right) \quad (4.10)$$

Although in theory, this can be measured using a single seismometer, Love wave contamination of the horizontal translational channels would distort any such measurement. As the horizontal rotational channels are insensitive to Love waves, they allow the extraction of  $\psi$  without such contamination.

#### 4.1.3 *single Station Dispersion Measurements*

As described in Section 2.7, two BRSs were installed at LHO, one at each end station located 5.66 meters apart.

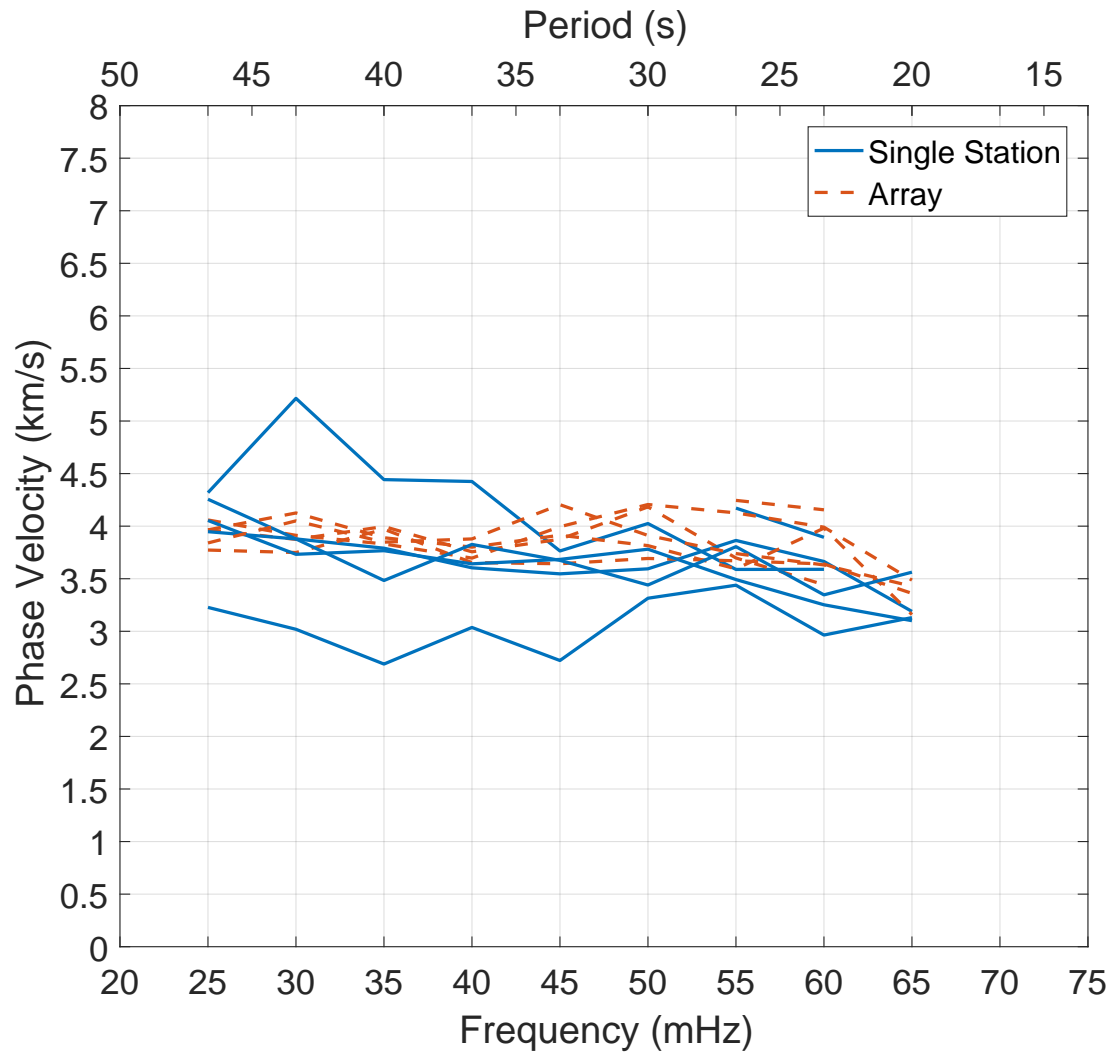


Figure 4.1: Rayleigh wave phase velocity measurements made by instruments located at the End-Y station of LHO, blue, and the same measurements achieved by the array of seismometers deployed at LHO. Each line represent the measurements achieved by different earthquakes. The angle of incidence of each wave was measured independent of the single station and used within the analysis. **cite tilt seismology**

## 4.2 Newtonian Noise

### 4.2.1 Theory

The gravitational coupling between the environment and an interferometer's test masses, so called Newtonian noise, is expected limit the performance of terrestrial gravitational wave detectors in the near future **CITE**. Sources of the gravitaitional field variations can range from atmospheric density changes to vibrations of the laboratory structures **CITE**. This coupling is unique in the fact that it can not be shielded or trivially engineered away. One can move an observatory underground to decrease the strength of the atmospherically driven fluctuations and those caused by seismic surface waves, discussed in detail in the following section. However, this process is both expensive and does not remove the sources which come from operating an instrument such as the vibrations of the vacuum structure or seismic motion sourced by laboratory equipment.

For the current surface-level interferometric observatories, the seismic motion due to Rayleigh waves is thought to be the dominant contributor to the Newtonian noise and will be the limiting noise source between **5-30 Hz** []. The motion due to a plane Rayleigh wave follows:

$$u_z(\mathbf{r}, t) = \alpha \cos(\zeta) \cos(\omega t - \mathbf{k} \cdot \mathbf{r} + \pi/2) \quad (4.11)$$

where  $\alpha$  is the amplitude,  $\zeta$  is the ellipticity angle,  $\psi$  is the angle of incidence in the horizontal plane,  $\omega$  is the frequency, and  $\mathbf{k} = \kappa(\cos(\psi), \sin(\psi), 0)$  is the wavevector. The corresponding test mass acceleration in the x-direction follows []:

$$a_x(\mathbf{r}, t) = 2\pi\alpha\gamma G\rho_0 e^{-h\kappa} \cos(\zeta) \cos(\phi) \cos(\omega t - \mathbf{k} \cdot \mathbf{r}) \quad (4.12)$$

where  $\gamma \approx 0.8$  is a factor which accounts for the counter-action of the change of density due to the seismic wave and the vertical motion of the ground.



### 4.2.2 *Observations*

## BIBLIOGRAPHY

- [1] Aasi, J. et al. (2015). Advanced ligo. *Classical and Quantum Gravity*, 32(7):074001.
- [2] Abbott, B. P. et al. (2019). Gwtc-1: A gravitational-wave transient catalog of compact binary mergers observed by ligo and virgo during the first and second observing runs. *Phys. Rev. X*, 9:031040.
- [3] B Arp, T., A Hagedorn, C., Schlamming, S., and H Gundlach, J. (2013). A reference-beam autocollimator with nanoradian sensitivity from mhz to khz and dynamic range of 10(7.). *The Review of scientific instruments*, 84:095007.
- [4] Belfi, J., Beverini, N., Carelli, G., Di Virgilio, A., Maccioni, E., Saccorotti, G., Stefani, F., and Velikoseltsev, A. (2012). Horizontal rotation signals detected by “g-pisa” ring laser for the mw = 9.0, march 2011, japan earthquake. *Journal of Seismology*, 16(4):767–776.
- [5] Einstein, A. and Rosen, N. (1937). On gravitational waves. *Journal of the Franklin Institute*, 223(1):43 – 54.
- [6] et. al., S. (2016). First deep underground observation of rotational signals from an earthquake at teleseismic distance using a large ring laser gyroscope. *arXiv*.
- [7] Haskell, N. A. (1953). The dispersion of surface waves on multilayered media. *Bulletin of the Seismological Society of America*, 43(1):17–34.
- [8] Lantz, B., Schofield, R., O’Reilly, B., Clark, D. E., and DeBra, D. (2009). Review: Requirements for a ground rotation sensor to improve advanced ligo. *Bulletin of the Seismological Society of America*, 99(2B):980–989.

- [9] Lee, W. H. K., Celebi, M., Todorovska, M. I., and Igel, H. (2009). Introduction to the special issue on rotational seismology and engineering applications. *Bulletin of the Seismological Society of America*, 99(2B):945–957.
- [10] Legendre, C. P., Zhao, L., Huang, W.-G., and Huang, B.-S. (2015). Anisotropic rayleigh-wave phase velocities beneath northern vietnam. *Earth, Planets and Space*, 67(1):28.
- [11] Lin, C.-J., Huang, H.-P., Pham, N. D., Liu, C.-C., Chi, W.-C., and Lee, W. H. K. (2011). Rotational motions for teleseismic surface waves. *Geophysical Research Letters*, 38(15):n/a–n/a. L15301.
- [12] Lin, F.-C., Moschetti, M. P., and Ritzwoller, M. H. (2008). Surface wave tomography of the western united states from ambient seismic noise: Rayleigh and love wave phase velocity maps. *Geophysical Journal International*, 173(1):281.
- [13] Maranó, S. and Fäh, D. (2014). Processing of translational and rotational motions of surface waves: Performance analysis and applications to single sensor and to array measurements. *Geophysical Journal International*, 196:317–339.
- [14] Matichard, F. et al. (2015). Seismic isolation of advanced ligo: Review of strategy, instrumentation and performance. *Classical and Quantum Gravity*, 32(18):185003.
- [15] Meier, T., Dietrich, K., Stöckhert, B., and Harjes, H. (2004). One-dimensional models of shear wave velocity for the eastern mediterranean obtained from the inversion of rayleigh wave phase velocities and tectonic implications. *Geophysical Journal International*, 156(1):45–58.
- [16] Pancha, A., Webb, T. H., Stedman, G. E., McLeod, D. P., and Schreiber, K. U. (2000). Ring laser detection of rotations from teleseismic waves. *Geophysical Research Letters*, 27(21):3553–3556.

- [17] Reinwald, M., Bernauer, M., Igel, H., and Donner, S. (2016). Improved finite-source inversion through joint measurements of rotational and translational ground motions: a numerical study. *Solid Earth*, 7(5):1467–1477.
- [18] Venkateswara, K., Hagedorn, C. A., Gundlach, J. H., Kissel, J., Warner, J., Radkins, H., Shaffer, T., Lantz, B., Mittleman, R., Matichard, F., and Schofield, R. (2017). Subtracting tilt from a horizontal seismometer using a ground rotation sensor. *Bulletin of the Seismological Society of America*, 107(2):709–717.
- [19] Venkateswara, K., Hagedorn, C. A., Turner, M. D., Arp, T., and Gundlach, J. H. (2014). A high-precision mechanical absolute-rotation sensor. *Review of Scientific Instruments*, 85(1).
- [20] Weiss, R. (1972). Electromagnetically coupled broadband gravitational antenna. In *K.S. Thorne, “Gravitational radiation”, 300 Years of Gravitation, S W Hawking and W Israel, pp 330–458*. University Press.